HHS Public Access

Author manuscript

Nat Microbiol. Author manuscript; available in PMC 2021 January 13.

Published in final edited form as:

Nat Microbiol. 2020 October ; 5(10): 1232–1246. doi:10.1038/s41564-020-0752-7.

Orally Efficacious Broad-Spectrum Allosteric Inhibitor of Paramyxovirus Polymerase

Robert M Cox[1], **Julien Sourimant**[1], **Mart Toots**[1], **Jeong-Joong Yoon**[1], **Satoshi Ikegame**[2], **Mugunthan Govindarajan**[3], **Ruth E Watkinson**[2], **Patricia Thibault**[2], **Negar Makhsous**[4], **Michelle J. Lin**[4], **Jose R Marengo**[3], **Zachary Sticher**[3], **Alexander A Kolykhalov**[3], **Michael G Natchus**[3], **Alexander L Greninger**[4], **Benhur Lee**[2], **Richard K Plemper**[1,*]

[1]Institute for Biomedical Sciences, Georgia State University, Atlanta, 30303 GA

[2]Department of Microbiology, Icahn School of Medicine at Mount Sinai, New York, NY 10029

[3]Emory Institute for Drug Development, Emory University, Atlanta, 30322 GA

[4]Virology Division, Department of Laboratory Medicine, University of Washington, Seattle, 98185 WA

Abstract

Paramyxoviruses such as human parainfluenza virus type-3 (HPIV3) and measles virus (MeV) are a substantial health threat. In a high-throughput screen for inhibitors of HPIV3, a major cause of acute respiratory infection, we identified GHP-88309, a non-nucleoside inhibitor of viral polymerase activity that possesses unusual broad-spectrum activity against diverse paramyxoviruses including respiroviruses (i.e. HPIV1 and HPIV3) and morbilliviruses (i.e. MeV). Resistance profiles of distinct target viruses overlap spatially, revealing a conserved binding site in the central cavity of the viral polymerase (L) protein that was validated by photoaffinity labeling-based target mapping. Mechanistic characterization through viral RNA profiling and *in vitro* MeV polymerase assays identified a block in the initiation phase of the viral polymerase. GHP-88309 showed nanomolar potency against HPIV3 isolates in well-differentiated human airway organoid cultures, was well-tolerated (selectivity index >7,111), orally bioavailable, and provided complete protection against lethal infection in a Sendai virus (SeV)-mouse surrogate model of human HPIV3 disease when administered therapeutically 48 hours after infection. Recoverees had acquired robust immunoprotection against reinfection and viral resistance coincided with severe attenuation. This study provides proof-of-feasibility of a well-behaved broad-spectrum allosteric

[*]**Correspondence** To whom correspondence and requests for materials should be addressed: Richard K Plemper, rplemper@gsu.edu.

Author contributions

R.M.C. performed and analyzed most of the experiments. J.S. performed RdRP assays. M.T. and J.-J.Y. assisted with animal and organoid studies. S.T., R.E.W., P.T., N.M., M.J.L., A.L.G., and B.L. performed NGS experiments and data analysis. M.G., J.R.M., Z.S., A.A.K., and M.G.N. performed chemical synthesis and PK analyses. R.K.P. contributed to HTS and biochemical experiments, and supervised the study.

Competing interests

R.M.C., B.L., and R.K.P. are co-inventors on provisional patent application “2-fluoro-6-isoquinolin-5-ylbenzamide, and Antiviral Uses Related Thereto”, covering method of use of GHP-88309 for paramyxovirus disease therapy. This study could affect their personal financial status. All other authors declare no competing interests.

antiviral and describes a chemotype with high therapeutic potential that addresses major obstacles of anti-paramyxovirus drug development.

Much-needed drug development against paramyxoviruses has been hampered primarily by three obstacles: the viruses cause predominantly acute disease[1,2], limiting the window of opportunity for intervention; only a fraction of patients can be expected to be open to treatment, restricting the size of treatable patient populations despite high disease prevalence; and a predominantly pediatric patient population complicates clinical trial design.

Exemplifying the problem is our previously identified MeV inhibitor with nanomolar potency, ERDRP-0519, that is orally efficacious against lethal morbillivirus infections when given post-exposure prophylactically[3]. Despite its potential to improve measles case management, clinical development against this re-emerging pathogen[4–6] has slowed due to perceived low economic potential of a measles drug and ethical challenges arising from highest disease burden in pre-teen pediatric patients[7–9].

Human viral challenge models with adult volunteers[10] established for related respiratory syncytial virus (RSV) facilitate trial design and have been used for clinical testing of small molecule RSV inhibitors[11]. Unfortunately, these models have not been fully predictive of clinical outcome[12,13], cannot be established for more pathogenic paramyxoviruses such as MeV, and are lacking for HPIVs.

Broad-spectrum anti-paramyxovirus drug candidates that inhibit at least one family member with predictable disease burden in adults may offer a viable path to establish clinical proof-of-concept; provide benefit to a larger patient pool suffering from diverse paramyxovirus infections to better offset developmental costs; and widen windows of opportunity against at least some indications, since disease progression profiles vary between paramyxoviruses. However, traditional broad-spectrum antivirals are host-directed[14–19] or ribonucleoside analogs[20–23] that are unlikely to meet the tight safety profile necessary for pediatric use and therefore make poor anti-paramyxovirus candidates overall. Allosteric direct-acting antivirals are better suited to deliver the required safety margin, but are typically restricted to a single paramyxovirus target.

Driven by the rationale that a sizeable adult patient population and viable treatment window will be paramount for advance to clinical testing, HPIVs represent a promising primary target for an anti-paramyxovirus drug screen. In addition to children, HPIVs pose a major threat to immune-compromised adults such as hematopoietic stem-cell transplant patients, among whom case-fatality rates can reach a staggering 75%[24,25]. HPIV disease progression in some adult at-risk groups appears to be relatively slow, reflected by a median 3 days for progression to severe lower respiratory tract infection after appearance of initial upper respiratory symptoms[24]. In this study, we therefore selected HPIV3, the predominant etiological agent of HPIV disease with an estimated 3 million medically-attended cases in the US annually[26,27], as the screening agent for a high-throughput antiviral drug discovery campaign. This screen identified GHP-88309, an orally efficacious broad-spectrum inhibitor of the paramyxovirus polymerase.

Results

We have pioneered an HTS protocol centered on a recombinant HPIV3 expressing nanoLuciferase (HPIV3-JS-NanoLuc) (Extended Data 1a). Fully validated (Extended Data 1b), we applied the protocol to screen 141,936 compounds. Combining control-dependent and independent statistical methods for hit identification (Fig. 1a), we admitted 451 compounds to direct and orthogonal counterscreens (Extended Data 1c; Supplementary Table 1). Performance requests were EC_{50} <1 μM, CC_{50} >20 μM, lack of reporter interference, and absence of chemotype promiscuity and chemical reactivity[28]. Two compounds, GHP-88309 and GHP-64627, met all criteria and were sourced. GHP-88309 (Fig. 1b) passed subsequent filters, returning active concentrations of 0.4–0.78 μM against recHPIV3-JS-NanoLuc after chemical re-synthesis (Fig. 1c–d), which was statistically indistinguishable (P=0.7233) from the sourced material (Extended Data 1d). Multi-day incubation of cells in the presence of up to 1 mM GHP-88309 revealed no cytotoxicity, corresponding to SIs >2,500 in uninfected (Fig. 1e; Extended Data 1e–f) and infected (highest concentration tested 300 μM; Extended Data 1g) cultured cells.

Chemotype with broadened anti-paramyxovirus activity spectrum

Inhibitory activity of GHP-88309 was not restricted to HPIV3 but included other members of the respirovirus genus tested (HPIV1, SeV) and extended to morbilliviruses (MeV, canine distemper virus (CDV)) (Fig. 1d; Supplementary Table 2). Paramyxoviruses of the more distantly related orthorubulavirus genus (HPIV2), pneumoviruses (RSV), and orthomyxoviruses (influenza A viruses) were not inhibited.

To test whether broad-spectrum activity of GHP-88309 was due to undesirable poly-pharmacologic behavior, we assessed compound aggregation or chemical reactivity[29–31] (Extended Data 2a). Only statistically insignificant (P=0.329) changes in antiviral potency (EC_{50}=0.59–1.16 μM) were noted in response to altered pH, varied amounts of virus inoculum, or bovine serum albumin added in high-concentration. Synthetic elaboration of the scaffold revealed a structure-activity relationship (SAR) that was consistent for HPIV3 and MeV targets (Supplementary Table 3) and indicates that GHP-88309 is not a singular hit but the founding member of a distinct antiviral chemotype.

GHP-88309 is bioactive in primary cells and against clinical isolates

When tested in disease-relevant human bronchial tracheal airway epithelial cell (HBTEC) cultures against HPIV3-JS and clinical isolates HPIV3–9R4 and HPIV3–10L3, antiviral potency was increased approximately 5-fold (EC_{50} 0.07 and 0.08 μM, respectively) in the primary cell/virus isolate system, whereas the low degree of GHP-88309 cytotoxicity remained unchanged (CC_{50} ~1 mM) (Fig. 1e). Both isolates had minimal laboratory exposure, having been amplified *ex vivo* for a maximum of two passages[32]. Expanded testing against an additional three HPIV3, three HPIV1, and six MeV clinical isolates on cultured cells demonstrated consistent antiviral potency across different target viruses and virus strains (Extended Data 2b–d).

Time-of-addition (ToA) variation studies using HPIV3 and MeV as targets provided initial insight into the antiviral mechanism of GHP-88309. Previously characterized MeV entry (AS-48)[33] and polymerase (ERDRP-0519)[3] inhibitors and host-directed RdRP blocker JMN3–003[34] served as references. GHP-88309 ToA profiles overlapped with those of the polymerase inhibitors ERDRP-0519 and JMN3–003 (Fig. 1f; Extended Data 2e). Follow-up minigenome reporter assays established for MeV-Edm, HPIV3-JS, and CDV-Onderstepoort revealed specific inhibition of viral RdRP activity by GHP-88309 (Fig. 1g), since an RSV-derived minigenome assay was not affected.

Resistance hot-spots locate to L protein

We determined resistance profiles of GHP-88309 for MeV, HPIV3, and – representing the challenge virus of our surrogate small-animal efficacy model – SeV. Dose-escalation viral adaptation (0.5–200 μM concentration range) was carried out in six series per target until viral growth in the presence of compound improved. Sanger and next-generation sequencing revealed mutations in the L proteins of all phenotypically-resistant HPIV3, SeV, and MeV populations (Fig. 2a; Supplementary Information Computational Data 1–18). Whole genome analysis of resistant HPIV3 populations showed no mutations in other viral protein components associated with the RdRP complex, the nucleocapsid (N) and phosphoprotein (P). Several substitutions affected the attachment and fusion glycoproteins, but these changes reportedly arise from HPIV3 adaptation to immortalized cell lines[32,35–38] and were not pursued. An L_{G1036E} polymorphism appeared in several SeV lineages after exposure to GHP-88309 or vehicle, suggesting a natural polymorphism or cell-culture adaptation effect. All other L mutations were rebuilt in respective HPIV3, SeV, or MeV minigenome systems and/or recombinant viruses and specific resistance sites identified (Extended Data 3a–d).

To structurally locate confirmed sites, we generated homology models of HPIV3, SeV, and MeV L based on a cryo-electron microscopy reconstruction of the related PIV5 L protein[39]. All validated sites clustered in a conserved L microdomain that lines the interior of the template channel near the intersection of the RdRP and capping domains (Fig. 2a–d), corresponding to the thumb domain of the polymerase complex. This tight and conserved spatial arrangement of resistance mutations suggests proximity to the physical target site of GHP-88309.

Photo-crosslinking target mapping and extraction of a docking pose

Informed by the emerging SAR, we designed a photo-activatable azide analog, GHP-88309–016 (Extended Data 4a), which maintained antiviral activity against HPIV3 and MeV in cell-based assays (Extended Data 4b). Using purified MeV L complexes (Extended Data 4c), we covalently photo-coupled GHP-88309–016 and identified docking sites through LC-MS/MS. Three distinct peptides contained an additional mass corresponding to the ligand (Supplementary Table 4; Extended Data 4d). Localization in the MeV L structural model suggested two of these peptides (Extended Data 4e) likely form non-specific cross-links reported for phenylazides such as GHP-88309–016[40,41], while residues 992–994 in peptide 3 form part of the central L cavity wall immediately proximal to the resistance cluster (Extended Data 4f).

Based on closest mutual proximity (Extended Data 5a), we selected residue D993 of peptide 3 and resistance sites E863, A866, S869, Y942, I1009, T1010, and Y1106 as targets for *in silico* docking. A conserved top-scoring pose for GHP-88309 and GHP-88309–016 placed the ligands at the interface of the capping and polymerase domains (Fig. 2e), bringing the aryl-azide functional group of GHP-88309–016 within ~8Å of residues 992–994 in peptide 3 (Extended Data 5b). The isoquinoline ring of GHP-88309 is predicted to form π-hydrogen bonds with L residues Y942 and R865, which are conserved in susceptible viruses, and the benzamide moiety is positioned within 5Å of residues Q1007 and R1011 (Extended Data 5c). This arrangement pharmacologically links the L capping and RdRP domains. Equivalent *in silico* GHP-88309 docking attempts to L proteins of uninhibited Nipah virus (NiV) and RSV failed to yield comparable binding poses (Extended Data 5d–e).

Resistance decreases inhibitor binding affinity

We employed biolayer interferometry (BLI) to monitor GHP-88309 affinity for purified MeV L immobilized on biosensors[42]. GHP-88309 binding to standard MeV L reached saturation (Extended Data 6a) and showed an affinity (K_D) of 6.2 μM, whereas binding to L proteins with *bona fide* resistance mutations (L_{S869P}, L_{I1009F}, L_{Y1106S}, $L_{S869P/Y942H}$) was drastically reduced (Fig. 2f; Supplementary Table 5). Substitution at a respirovirus resistance hot-spot, L_{E858D}, in the MeV L background, yielded only moderate escape. A ~10-fold difference between EC_{50} and K_D concentrations presumably reflects the conformational heterogeneity of paramyxovirus polymerase preparations, only a subset of which is bioactive and thus represented in the EC_{50} value.

Sequence database searches for HPIV3, HPIV1, and MeV L did not show natural polymorphisms at confirmed GHP-88309 resistance sites. An exception was a laboratory-generated temperature-sensitive HPIV3 vaccine candidate that is attenuated through L_{Y942H} mutation[43]. However, paramyxovirus genera containing sequence variations in the target microdomain, such as the orthorubulavirus HPIV2, were not inhibited by GHP-88309 (Supplementary Figure 1). Likewise, NiV L, which features a histidine at position 1156 homologous to the L_{Y1106H} resistance substitution in MeV and SeV, was uninhibited (EC_{50}=314.1 μM; Extended Data 6b). Introducing L_{H1156Y} mutation into NiV L conferred susceptibility to GHP-88309 (59-fold lower inhibitory concentration in minireplicon assays; EC_{50}=5.3 μM) (Extended Data 6b), indicating that the compound target site emerged structurally conserved from paramyxovirus evolution and acquired only isolated point mutations across different genera.

GHP-88309 impairs initiation of RNA synthesis

Quantification of relative viral mRNA amounts synthesized in infected cells during primary transcription revealed dose-dependent reduction of both HPIV3 and MeV mRNA by the compound (Fig. 2g–h; Extended Data 7a–c). This outcome could reflect suppressed phosphodiester bond formation, blocked L-mediated mRNA capping, or impaired RdRP initiation at the promoter. We tested aborted mRNA maturation by quantifying the effect of GHP-88309 on HPIV3- or MeV leader (Le)-RNAs, which are the first products of the viral transcriptase after cell entry[44]. The compound dose-dependently inhibited synthesis of Le-RNAs (Fig 2i; Extended Data 7d) but did not alter HPIV3 and MeV mRNA transcription

gradients (Extended Data 7e–f). These results are incompatible with impaired mRNA capping since i) mononegavirus Le-RNAs are neither capped nor polyadenylated and should therefore not be affected by blocked capping; ii) RdRPs in transcriptase mode abort when nascent mRNAs remain uncapped[45], which would result in a steepened viral transcription gradient.

We assessed inhibition of RdRP initiation versus RNA elongation in *in vitro* MeV RdRP assays based on purified recombinant polymerase complexes (Fig 2j; Supplementary Figure 2; Extended Data 8). A 25-mer synthetic RNA template explored effects of GHP-88309 on phosphodiester bond formation and elongation, taking advantage of an artificial back-priming step when the template spontaneously forms a circular hairpin structure (Fig. 2j; Extended Data 8a–b)[46,47]. GHP-88309 did not block RNA elongation after back-priming, and therefore does not prevent phosphodiester bond formation (Fig. 2j; Extended Data 8c). However, we noted dose-dependent inhibition of *de novo* RNA synthesis when using a 16-mer RNA template[48] that does not support back-priming (Extended Data 8d–e), albeit at considerably higher compound concentrations than EC_{50} values. Testing of a catalytically inactive L_{N774A} mutant confirmed specificity of the *in vitro* polymerase assay (Fig. 2j; Extended Data 8 c, e).

GHP-88309 is efficacious in disease-relevant 3D human airway organoids

In humans, HPIV3 infection typically remains localized to the respiratory tract[49]. To assess antiviral potency in a disease-relevant human tissue model, we generated well-differentiated primary human bronchial tracheal airway epithelium cultures grown at air-liquid interface (3D-ALI-HBTEC)[50]. Transepithelial electrical resistance (TEER)[51], and microscopically-examined tight junction organization were unchanged after organoid exposure to up to 640 μM GHP-88309 in the basolateral chamber (Fig. 3a–b), confirming a wide safety margin.

Dose-response curves generated for HPIV3 isolates 10L3 and 9R4, and HPIV1 isolate 5F6 returned EC_{50}s in the nanomolar range (90 nM, 105 nM, 280 nM, respectively) in 3D-ALI-HBTECs (Fig. 3c–d;). Confocal microscopy of infected and treated organoid cultures confirmed virus replication predominantly in ciliated cells, consistent with previous reports[52], and identified a static GHP-88309 concentration of 10 μM in the basolateral chamber as sterilizing (Fig. 3e).

Oral bioavailability of GHP-88309

Since established small-animal models of HPIV3 are only semi-permissive and none recapitulates all key features of human disease[53], we selected the SeV mouse surrogate model to monitor efficacy against respirovirus disease in a natural host[53]. Accordingly, PK profiles were determined in mice.

Metabolic stability testing in the presence of human and mouse liver microsomes showed long half-lives of 15.3 and >24 hours, respectively (Fig 4a). Single-dose PK assays in mice with 50 and 150 mg/kg oral GHP-88309 revealed a dose-dependent, albeit non-linear, overall drug exposure, sustained drug plasma concentrations >30 μM after a 150 mg/kg dose, and oral bioavailability approaching 90% (Fig 4b; Supplementary Table 6). Drug tissue distribution 60 minutes after plasma C_{max} corroborated high plasma stability, showing

GHP-88309 organ concentrations ranging 70–246 nmol/g in all soft tissues tested, including lung (Fig 4c). The compound was well tolerated in a 5-day multi-dose oral PK study with b.i.d. administration at 150 mg/kg. Exposed animals developed no signs of biotoxicity despite very high sustained drug plasma concentration that plateaued at ~34 μM at trough – equivalent to 17-times the cell culture EC_{50} for SeV – over a 4-day treatment period (Fig 4d). Multi-day dosing did not significantly ($P>0.82$) alter PK properties of GHP-88309 (Fig 4e).

GHP-88309 is orally efficacious in HPIV disease surrogate model

SeV in mice recapitulates HPIV pathology[53], but mice succumb to infection within 8–10 days, establishing a concise therapeutic endpoint. Since cell culture EC_{90} concentrations of GHP-88309 were ~6–17–fold lower against HPIV3, HPIV1, and MeV than SeV, the SeV/mouse system promises to be a robust predictor of antiviral efficacy.

GHP-88309 was administered orally at 150 mg/kg b.i.d., starting at the time of infection (prophylactically) or 48 hours post infection (pI), when lower respiratory tract disease was established[54,55] (therapeutically). Both regimens alleviated body weight losses and prevented hypothermia (Fig 5a–b). All treated animals survived, whereas mice of the vehicle-treated group succumbed (predefined endpoint >20% loss of body weight) within 9 days (Fig 5c). Treatment significantly reduced virus load in trachea (Fig 5d; $P_{therapeutic}=0.0068$ and $P_{prophylactic}<0.0001$) and lungs (Fig 5e; $P<0.0001$).

Histological assessment of lung sections six days pI revealed cellular infiltrates in vehicle-treated animals, coinciding with bronchiolar inflammation (Fig 5f–g). Lung sections of prophylactically treated animals showed no statistically significant ($P=0.62$) pathological changes. Inflammation and cellular infiltrates were alleviated in lungs of animals treated therapeutically.

Treatment results in pharmacological virus attenuation

We determined the relative induction of signature genes of the host innate antiviral response in lung tissue three, six, and nine days pI (Fig 5h; Extended Data 9a). IFN-β induction, which is directly correlated with SeV pathogenesis[56], was significantly lower ($P_{therapeutic}=0.0088$; $P_{prophylactic}=0.0011$) in treated mice on day 3 pI than in vehicle animals. *Ex vivo* treatment of HPIV3-infected HBTECs with GHP-88309 did not reduce IFN-β levels (Extended Data 9b), confirming no direct interference with IFN expression.

Paramyxovirus nonstructural proteins, C and V in the case of SeV, counteract host antiviral responses[57,58]. Mice in treatment groups showed increased IL12b expression on day 3 despite a lower virus burden than in untreated animals, indicating unmitigated host immune activation and thus direct pharmacological virus attenuation by GHP-88309. By day 6, however, treated animals showed significantly decreased expression of inflammatory markers (IL-6 ($P_{prophylactic}=0.0265$), TNF ($P_{prophylactic}=0.0329$ and Acod1 ($P_{prophylactic}<0.0001$, $P_{therapeutic}=0.020$)) and of some interferon stimulated genes (isg15, slfn4) with antiviral effector function. Infected, treated HBTECs shows enhanced ISG expression (Extended Data 9b), consistent with unmitigated IFN-β signaling pathways.

Strong adaptive immunity in recoverees

Altered immune responses to paramyxovirus and pneumovirus infection can lead to exacerbated atypical disease upon rechallenge, as described for formalin-inactivated experimental MeV[59] and RSV vaccines[60]. To assess the impact of treatment experience on downstream pathogenesis, we designed a rechallenge study (Fig 6a). SeV-infected animals were treated therapeutically, starting 48 hours pI, for 9 days b.i.d. Treatment significantly alleviated clinical signs (Fig 6b–c) and all animals survived, whereas controls succumbed (Fig 6d). Recoverees mounted a robust humoral anti-SeV response (Fig 6e). Subsequent rechallenge with 1.5×10^5 $TCID_{50}$ SeV 28 days after original infection resulted in complete survival without development of clinical signs (Fig 6f–h), while a fresh group of naïve animals succumbed.

GHP-88309 resistant viruses are apathogenic

To explore whether resistance to GHP-88309 coincides with infection rebound, we rebuilt all confirmed SeV L resistance mutations in recombinant viruses. In cell culture, these recSeVs showed significant growth delays ($P<0.0013$) compared to the parent virus (Fig 6i). Three recSeVs were selected for *in vivo* testing, based on diversity in hot-spot location, best relative fitness in cell culture, and cross-appearance in HPIV3 (recSeV-L_{E863D}) and MeV (recSeV-L_{I1009L} and recSeV-L_{Y1106S}) adaptations. All animals infected with these viruses survived with only minimal weight loss (Fig 6j–k). Lung virus load was reduced or below detection level six days pI, when standard recSeV titers peak, and two resistant viruses had reverted to wild-type L (Supplementary Table 7).

To explore whether *in vivo* virus adaptation identifies additional escape mutations, we passaged recSeV twice in mice treated with sub-inhibitory 50 mg/kg GHP-88309. Of five independent lineages, virus was undetectable in two after the second passage. Viruses isolated from the other three lineages showed unchanged susceptibility to GHP-88309, and Sanger sequencing of L regions associated with resistance did not reveal polymorphisms at known escape sites (Supplementary Table 7). These results indicate that SeV resistance to GHP-88309 coincides with strong viral attenuation *in vivo*. Although a combination of multiple compensatory mutations may restore fitness of a GHP-88309-resistant virus, a high barrier exists against viral escape without corresponding loss of pathogenicity.

Discussion

Most allosteric small-molecule antivirals show a narrow activity spectrum[3,61–67]. For the mononegaviruses, antiviral activity spanning more than one genus has not yet been reported for any direct-acting non-nucleoside inhibitor. The discovery of GHP-88309 has shifted this paradigm. Based on sequence alignments, we predict that all respiroviruses and morbilliviruses are susceptible. Obviously, NiV is not inhibited due to a histidine at L_{1156}, but some members of the henipavirus genus such as Cedar virus or Ghanaian bat virus feature a tyrosine and may be sensitive.

Natural resistance of NiV to the drug raised the question of whether use against respiroviruses and morbilliviruses may trigger resistance mutations that make these viruses

more NiV-like, possibly resulting in enhanced disease. Tested in the recSeV-mouse pathogenesis model, all SeV resistance mutations resulted in major viral attenuation, alleviating pathogenesis concerns.

Mechanistic studies consistently pointed at impaired *de novo* polymerase initiation at the promoter by GHP-88309, reflecting a powerful strategy to block paramyxovirus polymerases. Whereas some inhibitors of related viruses such as RSV-restricted AZ-27 suppress *de novo* polymerase initiation[65], resistance profiles and predicted target sites of GHP-88309 and AZ-27 are distinct (Extended Data 10). Our top-scoring docking pose posits GHP-88309 at the intersection between the RdRP and capping domains, a prime location to prevent structural rearrangements required for polymerase processivity[68] by bridging both domains. Of note, escape mutations to a series of RSV capping inhibitors[69] map to polymerase regions distinct from GHP-88309 resistance (Extended Data 10), underscoring that GHP-88309 does not directly interfere with viral mRNA capping.

PK profiling of GHP-88309 demonstrated that outstanding oral bioavailability and metabolic stability readily compensated for moderate potency deficiencies. Although not dosed to failure yet, even the current orally efficacious 150 mg/kg correspond to a not unrealistic 12 mg/kg human equivalent[70] dose. In contrast to the morbillivirus polymerase inhibitor ERDRP-0519[3], GHP-88309 did not trigger major increase in ISG expression levels compared to vehicle in the SeV model, which may reflect that SeV infection is limited to respiratory epithelial cells whereas morbilliviruses cause viremia. GHP-88309 provides a unique foundation to dissect the impact of pharmacological intervention with localized and systemic paramyxovirus infections in relevant surrogate models.

Considering the broadened activity spectrum of GHP-88309 and high HPIV disease burden in immunocompromised adults, the compound addresses major concerns that have impaired clinical development of paramyxovirus drugs. Providing a viable path to efficacy assessment, trials could involve adult transplant recipients suffering from devastating HPIV3 infection[24,25]. In addition to a perceived expanded window of opportunity for therapeutic intervention[24], frequent monitoring of this group allows for early detection of infection. Our data showcase strong therapeutic potential of the GHP-88309 chemotype, which combines large safety margins with demonstrated oral efficacy, opening opportunities to ultimately address the currently unmet clinical need of patients suffering from respirovirus or morbillivirus disease.

Methods

Cells

Human carcinoma (HEp-2, ATCC CCL-23), human embryonic kidney (293T, ATCC CRL-3216), human bronchial epithelial (BEAS-2B, ATCC CCL-9609), human Madin Darby canine kidney (MDCK, ATCC CCL-34), African green monkey kidney epithelial cells (CCK-81; ATCC) stably expressing human signaling lymphocytic activation molecule (Vero-hSLAM) or canine signaling lymphocytic activation molecule (Vero-cSLAM) were maintained at 37°C and 5% CO_2 in Dulbecco's modified Eagle's medium (DMEM) supplemented with 7.5% fetal bovine serum. HEp-2 cells are indicated in the ICLAC

database of commonly misidentified cell lines, use of these cells is necessary since they are highly permissive for respiratory syncytial virus. Normal primary Human Bronchial Tracheal Epithelial Cells (HBTECs; Lifeline Cell Technology) were propagated and maintained in BronchiaLife Cell Culture Medium at 37°C and 5% CO_2. HBTECs were analyzed for microbial contamination by LifeLine Cell Technology. Insect cells (SF9) were propagated in suspension using Sf-900 II SFM media (Thermo Scientific). Human peripheral blood mononuclear cells (Fisher) were cultured in RPMI-1640 and stimulated with 0.2 μg of phytohemagglutinin (PHA; Sigma) for 24 h prior to use. All immortalized cell lines used in this study are routinely checked for mycoplasma and microbial contamination. GeneJuice transfection reagent (Invitrogen) was used for transfections unless otherwise stated.

Molecular biology

All modifications to Respirovirus reverse genetics plasmids (recSeV and recHPIV3) were performed as previously described[71], with PCR amplification of insert fragments using CloneAmp 2×PCR Master mix (Takeda). recSeV-Fushimi-Gluc-P2A-eGFP was derived from recSeV-Fushimi-eGFP (recSeV-eGFP), replacing the eGFP reporter with the previously-reported Gluc-P2A-eGFP reporter cassette from recHPIV3-JS-GlucP2AeGFP. recHPIV3-JS-NanoLuc was derived from recHPIV3-JS-GlucP2AeGFP by replacing the Gluc-P2A-eGFP reporter cassette with the NanoLuc open reading frame from pNL1.1.CMV [Nluc/CMV] (Promega). For minigenome studies, potential resistance mutations were cloned into MeV-Edm and HPIV3-JS L plasmids under T7 control using PCR mutagenesis. All plasmids were sequenced to confirm resistance mutations and sequence integrity. For generation of the baculovirus protein expression system used for RdRP assays, MeV (strain IC-B) L and P genes were codon optimized and cloned into the Fastbac dual vector (ThermoFisher Scientific). MeV L was expressed under the polyhedron promotor and MeV P with a C-terminal His-tag was expressed under the P10 promoter. To generate the baculovirus expression system used for purification of the C-terminal MeV L fragment L_{1708}, MeV L_{1708} (encoding for aa1–1708 of MeV L, with C-terminal FLAG and His tags) was codon optimized and cloned into the Fastbac dual expression system along with MeV P.

Viruses

Recovery of recombinant respiroviruses was carried out as previously described[71]. recHPIV3-JS NanoLuc was amplified on HeLa cells at 32°C, purified on a 60% sucrose cushion, and further purified on a 25%−65% sucrose gradient. MeV/Alaska.USA/16.00 (MeV-Anc), recCDV-5804p, and recRSV stocks were propagated on Vero-hSLAM, Vero-cSLAM, and HEp-2 cells respectively (multiplicity of infection (MOI) 0.01 $TCID_{50}$ units/cell). A single freeze-thaw cycle was used to release cell-associated progeny virions. The identity of rescued viruses was confirmed through Sanger sequencing after RT-PCR, using appropriate primers. Progeny titers of MeV, CDV, recHPIV3-JS-NanoLuc, RSV, or SeV virus titers were determined by $TCID_{50}$ titration on Vero-hSLAM, Vero-cSLAM, Vero-E6, HEp-2 cells, Vero-E6 cells respectively. Titers of clinical of HPIV3 and HPIV1 isolates were determined by $TCID_{50}$-HA titration on Vero-E6 cells followed by HA assay using guinea pig red blood cells[72]. To generate multi-step virus growth curves, Vero-E6 cells (approximately 1×10^5 per well in a 24-well plate format) were infected with recHPIV3 or

recSeV as specified (MOI 0.01 $TCID_{50}$ units/cell). Inocula were replace with fresh growth media after one hour, infected cell aliquots harvested every 12 hours, and released viral titers determined through $TCID_{50}$ titration.

HTS and hit identification

A total of 141,936 compounds were screened for inhibitory activity against recHPIV3-JS NanoLuc (MOI = 0.2 $TCID_{50}$ units/cell). HTS was carried out analogous to our previous reports[64,73], with automated reading of plates 30 hours after infection. Raw data were imported into the MScreen IT environment and analyzed using data mining tools developed in-house or build into the MScreen package as described[64,73]. Hit candidates were defined as compounds with anti-HPIV3 active >2.66×SD in control-dependent mean percent inhibition calculation and >2.1×SD in control-independent mean robust z-score calculation.

Counterscreens

For counterscreens, compound was added in 3-fold dilutions (0.009–20 μM) to 96 well plates seeded with Vero-E6 cells (1.1×10^4/well), followed by infection with recHPIV3-JS-NanoLuc, recMeV-NanoPEST, recSeV-Fushimi-Gluc-P2A-eGFP, recVSV-NanoLuc, or RSV A2-L19F$_{D489E}$fireSMASh reporter viruses (MOI = 0.2 $TCID_{50}$ units/cell) and automated plate reading 30 hours after infection. To triage reporter-interfering candidates, duplicate plates were infected with recVSV-NanoLuc (MOI = 0.2 pfu/cell). Cytotoxic concentrations were determined in equivalent serial dilution plates after exposure of uninfected cells for 30 hours to the test article, followed by addition of PrestoBlue substrate (Invitrogen) to quantify cell metabolic activity as described[64]. Four-parameter variable slope regression was used to determine EC_{50}, EC_{90}, and CC_{50} concentrations. To determine potential chemical liabilities and compound promiscuity, hit candidates were processed *in silico* through PAINS filters (www.swissadme.ch) and aggregation predictions using Badapple (http://pasilla.health.unm.edu/tomcat/badapple/badapple). To measure potential promiscuous activities or chemical liabilities of GHP-88309, dose-response assays were carried out under altered conditions: i) cells in dose-response plates were infected with high amounts of recHPIV3-JS-NanoLuc (MOI 3 $TCID_{50}$ units/cell); ii) to measure non-specific off-target aggregation effects, GHP-88309 was diluted in DMEM containing 10% FBS and 10mg/mL bovine serum albumin, and the dilutions added to cells after 30-minute preincubation followed by infection; and iii) 3-fold dilutions of GHP-88309 were generated at different media pH values (pH 5.5, 6.5, 8.3). In all cases, luciferase activity was measured after incubation of cells for 30 hours at 37°C in 5% CO_2 environment. For virus yield-based dose response assays, cells were infected (MOI=0.1 $TCID_{50}$ units/cell) in a 24-well plate format with recHPIV3-JS NanoLuc, recMeV-Anc, recCDV-5804, recSeV-Fushimi-eGFP, MeV, HPIV1, HPIV2, or HPIV3 in the presence of serial compound dilutions. Titers of progeny cell-associated (MeV and CDV) or released virions (recSeV-Fushimi, HPIV1, HPIV3) were determined 48 hours after infection through $TCID_{50}$ titration. The MitoBiogenesis in-cell ELISA (Abcam) was used according to the manufacturer's instructions to measure mitochondrial and cellular toxicity after incubation of HBTECs for 72-hour with GHP-88309. To assess whether mitotoxicity in cultured cells was masked by the Crabtree effect, VeroE6 were grown in galactose media as alternative carbohydrate sources, followed by PrestoBlue-based assessment of metabolic activity as outlined.

Minigenome reporter assays

HPIV3 and NiV derived minigenomes were NanoLuciferase, MeV and CDV minigenomes firefly luciferase based as described[64]. The NiV minigenome was modified to encode a NiV specific P-mRNA editing site inserted at the beginning of the Nanoluciferase open reading frame, ensuring that a functional Nanoluciferase mRNA was only produced after mRNA editing by NiV L. Reporter activities were determined in the presence of three-fold serial dilutions of GHP-88309 starting from 300 μM for NiV, 100 μM for HPIV3 and MeV, and 20 μM for CDV. Inhibitory concentrations were calculated as above.

Time-of-addition variation studies

Vero-E6 or Vero-hSLAM cells were infected (MOI=2 $TCID_{50}$ units/cell) with recHPIV3-JS-NanoLuc or recMeV-NanolucPEST, respectively. At the specified time points relative to infection, compounds (GHP-88309, JMN3–003, AS-48, or ERDRP-0519) were added to the culture media at a final concentration of 20 μM. Reporter gene expression was measured at 24 hours after infection.

HPIV3 metagenomic NGS library generation and antiviral resistance analysis

Metagenomic sequencing libraries were performed as described previously[74]. Viral RNA was treated with Turbo DNase I (Thermo Fisher). cDNA was generated from random hexamers using SuperScript III reverse transcriptase, and second strand was generated using Sequenase 2.0. Double-stranded cDNA was purified using Zymo DNA Clean and Concentrator. Sequencing libraries were generated using two-fifths volumes of Nextera XT on ds-cDNA with 20 cycles of PCR amplification. Libraries were cleaned using 0.8×Ampure XP beads and visualized on a 1.2% agarose FlashGel and pooled equimolarly before sequencing on an Illumina MiSeq (1×192bp run). Raw fastq reads were trimmed using cutadapt (-q 20) (https://doi.org/10.14806/ej.17.1.200). To interrogate potential resistance alleles, a Longitudinal Analysis of Viral Alleles (LAVA - https://github.com/michellejlin/lava) was carried out in a custom analysis pipeline. LAVA constructs a candidate reference genome from early passage virus using bwa[75], removes PCR duplicates with Picard, calls variants with VarScan[76], and converts these changes into amino acid changes with Annovar[77]. LAVA output HTML visualizations of minor allele changes with AF >5% and read depth >20× is provided in Supplementary Information files (Plemper_Supplementary_Analysis_1.html) to (Plemper_Supplementary_Analysis_12.html). Sequencing reads for the HPIV3 NGS campaign are available in NCBI BioProject PRJNA561835.

SeV L gene NGS

RNA extracts from infected cells were reverse transcribed and amplified by SuperScript III One-step RT-PCR kit (Invitrogen) by primer set of ‘L-amplicon f1’ and ‘L amplicon r8’, amplifying 1155–4266 (counted from L gene initiation codon) nucleotides of the L gene. Using this as a template, nested PCR was done to create 8 amplicons (400–450 bp) for NGS. Amplified 8 amplicons were mixed together and submitted to NGS. DNA library preparations, sequencing reactions, and initial bioinformatics analysis were conducted at GENEWIZ, using throughout NEBNext Ultra DNA Library Prep kit reagents following the

manufacturer's recommendations (Illumina). End repaired adapters were ligated after adenylation of the 3´ ends. Pooled DNA libraries were loaded on the Illumina instrument according to manufacturer's instructions and sequenced by MiSeq on a 2×250 paired-end (PE) configuration. Base calling was conducted by the Illumina Control Software (HCS) on the Illumina instrument. Paired-end fastq files were merged by BBTools and aligned to the reference sequence (8 amplicons tandemly connected) using bowtie2. BAM files created by bowtie2 were processed by IGVtools for variant detection. Complete sequencing results are shown in Supplementary Information files (Plemper_Supplementary_Analysis_13.html) to (Plemper_Supplementary_Analysis_18.html). The complete SeV NGS results are on the GEO database (GSE140376).

qRT-PCR analyses of viral and cellular transcripts

For MeV transcripts, Vero-hSLAM cells were infected with recMeV-Anc (MOI = 3 $TCID_{50}$ units/cell) and incubated in the presence of the GHP-88309, ERDRP-0519, or vehicle (at 37°C for 3–6 hours, or infected with recMeV-Anc (MOI = 0.2 $TCID_{50}$ units/cell) and incubated in the presence of control for 12 hours. For HPIV3 transcripts, VeroE6 cells were infected with recHPIV3-JS NanoLuc (MOI = 3 $TCID_{50}$ units/cell) and incubated in the presence of GHP-88309 or vehicle at 37°C for 2–4 hours. Total RNA was extracted at specified time points using Trizol and subjected to reverse transcription using either oligo-dT, MeV or HPIV3 leader-specific, or MeV or HPIV3 antigenome-specific primers as specified. Subsequent qPCR used primer pairs specific for a fragment in the MeV leader RNA, MeV antigenomic RNA, MeV P mRNA, MeV H mRNA, MeV L mRNA, HPIV3 N mRNA, HPIV3 antigenomic mRNA or human GAPDH mRNA, respectively, and samples were normalized for GAPDH. To determine induction of type-1 IFN pathways in HBTECs after HPIV3 infection, cells were infected with recHPIV3-JS NanoLuc (MOI = 1 $TCID_{50}$ units/cell) and incubated in the presence of GHP-88309 (6 μM) or vehicle at 37°C. RNA was isolated 16 hours after infection, and cDNA generated as above. qPCR used primer pairs specific for a fragment in human *ifit1, ifn-α, isg15, mx-a*, or human *gapdh*. Mock-infected and compound treated cells were used to determine whether GHP-88309 alone stimulates type-1 IFN pathways. For cytokine profiling of mouse lung tissues, relative *ifn-β, ifn-γ, acod1, il6, tnf, cxcl15, il12b, ddx60, gbp2, ifit3, isg15, slfn4,* and *sp100* mRNA concentrations were determined from total lung RNA extracts, generated 3, 6, and 9 days after infection of mice with recSeV-Fushimi-eGFP. Murine GAPDH mRNA as internal standard, and relative mRNA induction was calculated compared to lung tissues extracted from mock-infected animals. Heat maps were generated based on significant differences between vehicle and GHP-88309-treated animals.

In vitro MeV polymerase assay

MeV P and L proteins expressed in a baculovirus/insect cell system (Fastbac dual expression system and SF9 cells) were purified by Ni-NTA affinity chromatography after lysis of cells in 20 mM imidazole, 50 mM NaH_2PO_4, pH 7.5, 150 mM NaCl, 0.5% NP-40 buffer at 76 hours after infection. Proteins were eluted in 250 mM imidazole, 50 mM NaH_2PO_4, pH 7.5, 150 mM NaCl, 0.5% NP-40, followed by buffer exchange to 150 mM NaCl, 20 mM Tris-HCl, pH 7.4, 1 mM DTT and 10% glycerol with Zeba spin columns. Aliquots of purified P-L hetero-oligomers containing 100 ng of L were diluted in reaction buffer containing 1 mM

DTT, 10% glycerol, 50 mM Tris pH7.4 and mixed with 1 mM of ATP, UTP and CTP, 50 μM GTP, 10 μCi of $\alpha-^{32}$P labelled GTP (Perkin Elmer), 2 μM of RNA template (Dharmacon), variable amounts of $MnCl_2$ or $MgCl_2$ as specified in the figures, and 1% DMSO containing GHP-88309 at the specified concentration. Reactions were incubated at 30°C for 3 hours, RNAs ethanol-precipitated, resuspended in 50% deionized formamide with 10 mM EDTA, heat-denatured at 95°C for 5 minutes, and fractionated through 20% polyacrylamide gels containing 7 M urea in Tris-borate-EDTA buffer. Polymerization products were visualized through autoradiography. Molecular weight markers of 4, 16 and 25 nt were generated by labeling the 16 or 25 nt templates or a 4 nt synthetic RNA (ACCA) with $\gamma-^{32}$P-ATP, using T4 Polynucleotide Kinase (New England Biolabs).

Biolayer interferometry

Purified MeV L_{1708} was biotinylated using EZ-Link NHS-Biotin (ThermoFisher). After biotinylation, excess biotin was removed, and buffer exchanged to Octet Kinetics buffer (Fortebio) using a Zeba desalting spin column. Purified, biotinylated MeV L_{1708} preparation were bound to Super Streptavidin (SSA) high-binding biosensors (Fortebio) and dipped into increasing concentrations of GHP-88309 (1.2 μM to 300 μM) followed by dipping back into Kinetics buffer to generate small-molecule binding and dissociation curves. Reference sensors loaded with mouse anti-FLAG IgG and additional biocytin blocked sensors were used as double parallel controls for nonspecific binding. Global fitting of binding kinetics was used to determine K_D values using the Octet Red software package by Pall ForteBio. To visualize whether saturation of binding was reached, concentration-dependent steady-state sensor response signals were plotted (Extended Data 6a). Local K_D fittings based on the steady-state signals were identical to those derived from global fittings within the experimental margin of error (SD).

Photoaffinity labeling of GHP-88309–016 to MeV L_{1708}

Purified MeV L_{1708} was incubated with the photoreactive analog (GHP-88309–016 [40μM]) for 15 minutes prior to activating the crosslinker. The MeV L_{1708} -GHP-88309–016 mixture was placed on ice and exposed to UV light (365 nm) for 30 min, followed by an additional exposure to UV light (254 nm) for 15 minutes. Protein was then harvested using FLAG resin and subsequently incubated with Laemmli buffer at 56°C for 15 minutes. SDS-PAGE electrophoreses was then performed using Laemmli buffer on 4–15% acrylamide gels. Bands of interest were excised and analyzed by mass spectrometry. Crosslinked peptides were identified by the Proteomics & Metabolomics Facility at the Wistar Institute.

LC-MS/MS Analyses and Data Processing

Liquid chromatography tandem mass spectrometry (LC-MS/MS) analysis was performed by the Proteomics and Metabolomics Facility at the Wistar Institute using a Q Exactive Plus mass spectrometer (ThermoFisher Scientific) coupled with a Nano-ACQUITY UPLC system (Waters). Gel bands containing MeV L_{1708} were excised, digested in-gel with trypsin and injected onto a UPLC Symmetry trap column (Waters). Tryptic peptides were separated by reversed phase HPLC on a BEH C18 nanocapillary analytical column. Eluted peptides were analyzed by the mass spectrometer set to repetitively scan m/z from 300 to 2000 in positive ion mode. The full MS scan was collected at 70,000 resolution followed by data-

dependent MS/MS scans at 17,500 resolution on the 20 most abundant ions exceeding a minimum threshold of 20,000. Peptide match was set as preferred, exclude isotopes option and charge-state screening were enabled to reject unassigned charged ions. Peptide sequences were identified using pFind 3.1.5[78]. MS/MS spectra were searched against a custom database containing MeV L, Sf9, and Baculovirus, and protein sequences. Search parameters include full tryptic specificity with up to three missed cleavages, peptide mass tolerance of 10 ppm, fragment ion mass tolerance of 15 ppm, static carboxamide-methylation of cysteines, and variable oxidation of methionines. To identify GHP-88309–016 crosslinked peptides, mass addition of 261.0902 (MW of GHP-88309–016) was considered for all amino acid residues.

In silico Docking

Docking studies were performed with MOE 2018.1001, using the Amber10 force field. A native structure of RSV L (PDB 6pzk) and homology models of MeV and NiV L based on the coordinates reported for HPIV5 L (PDB 6v85) were used for docking studies. After protonation and energy minimization, an induced-fit protocol was used to dock the GHP-88309 in the L structures based on resistance data information. For MeV L, residues E858, E863, D997 (crosslinked peptide), I1009, T1010, and Y1106 were selected to identify the target site for docking, and resulting docking poses from each polymerase target compared. Homologous residues in RSV and NiV were selected to perform in silico docking into their respective L proteins.

Ex vivo metabolic stability of GHP-88309

To determine stability in plasma, GHP-88309 was incubated in triplicate in pooled human or CD-1 mouse plasma (BioIVT) in glass tubes in a 37°C shaker-incubator (150 rpm). Procaine and benfluorex served as positive controls and were analyzed in parallel. Aliquots were taken after 0, 5, 15, 30, 60 and 120 minute incubation time, mixed with 400 μL of internal standard in acidified (0.1% (v/v) formic acid) acetonitrile solution, clarified by centrifugation and supernatants analyzed by LC-MS/MS. To determine stability in liver microsomes, GHP-88309 was incubated in triplicate in glass tubes in 50 mM Tris-HCl (pH 7.5) buffer with 8 mM $MgCl_2$, 25 μg/mL alamethicin, Phase I and Phase II cofactors (NADPH regenerating system (NRS) and 2 mM UDPGA, respectively) and 0.5 mg total protein pooled mixed gender human liver microsomes (BioIVT) or pooled CD-1 mouse liver microsomes (Xenotech) in a 37°C shaker incubator (150 rpm). Verapamil served as Phase I positive control, negative controls lacked cofactors and contained 2% (w/v) $NaHCO_3$ in water instead of NRS. Aliquots were taken after 0, 15, 15, 30, 60 and 120 minutes and processed as outlined above.

All animal studies

Standard group sizes were 5 animals each, unless otherwise stated. Power calculation ($P<0.05$; 80% power) revealed that this sample size will detect differences in mean virus titer >0.71 logarithmical units. Animals were assigned to the different study groups randomly; no blinding of investigators was performed other than for histopathology scoring of lung sections.

Pharmacokinetics analysis in mice

All *in vivo* experiments were carried out in eight-week-old female 129×1/SvJ mice (Jackson Laboratory); as a minimum, animals were monitored once daily. Single-dose PK studies were carried out after i.v. and oral substance administration. For i.v. dosing, GHP-88309 was formulated in 28% PEG200, 5% dimethylacetamide, 67% 30% HPB cyclodextrin in sterile PBS at 1.25 mg/ml. For oral dosing, compound was formulated in 1% methylcellulose in water for a homogeneous suspension of up to 18.76 mg/ml. Mice were administered either 5 mg/kg via tail vein injection, or 50 mg/kg or 150 mg/kg via oral gavage, followed by blood collection after 0, 0.083, 0.25, 0.5, 1, 2, 4, 8 and 24 hours (i.v. group) or 0, 0.25, 0.5, 1, 2, 4, 6, 8 and 24 hours (per oral group). Plasma was prepared from whole blood (2000×g, 5 minutes, 4°C) within 15 minutes of blood collection and samples stored at −80°C until analysis by LC-MS/MS. Calibration curve range was 10–10,000 ng/ml, samples above quantitation limit were diluted with commercial CD-1 mouse plasma and retested. Quality control samples were interspersed throughout the run, and no chromatographic interferences were detected in blank CD-1 or 129×1/SvJ mouse plasma. For multi-dose PK studies, mice received GHP-88309 orally at 150 mg/kg dose concentration in a b.i.d. regimen for five days. In the first 4 days of dosing, blood samples were collected 0.5 hours (C_{max}) and 11.5 hours (trough) after the morning dose. On day 5, a full PK study (lacking the 6-hour time point) was performed after the morning dose as outlined. Blood samples were processed and analyzed as above. To determine GHP-88309 organ distribution, mice were administered a single oral dose of GHP-88309 at 150 mg/kg. Selected organs (brain, lung, spleen, kidney, liver, and heart) were extracted 90 minutes after dosing, flash frozen in liquid nitrogen, and stored at −80°C until further analysis by LC-MS/MS as described.

Determination of neutralizing antibody titers

Plasma was prepared as above, heat inactivated, serially diluted (2-fold steps) in serum free DMEM, mixed with 100 $TCID_{50}$ units of recSeV-Fushimi-eGFP, and incubated for one h at 25°C. Mixtures were transferred to Vero-E6 cell monolayers and virus neutralization measured after three days by visualization of GFP positive infected cells. Equal amounts of recSeV-Fushimi-eGFP in FBS, DMEM containing 7.5% FBS, and serum-free DMEM served as controls. Each blood sample was tested in two technical repeats.

Efficacy studies in the SeV mouse model

Challenge virus was recSeV-Fushimi eGFP, administered intranasally at 1.5×10^5 $TCID_{50}$ units in 50 μl of PBS. Prophylactic treatment with GHP-88309 commenced 2 hours before infection, therapeutic treatment was started 48 hours after infection. For all treatment studies, drug was administered per oral gavage in a b.i.d. regiment at 150 mg/kg body weight. Infected mice were monitored twice daily for clinical signs (body weight loss, body temperature change, overall composure). Lung and trachea viral titers were determined in groups of mice on days 3, 6, and 9 after infection through $TCID_{50}$ titration of tissue homogenates on Vero-E6 cells. Tissue samples for qRT-PCR were preserved in RNAlater until analysis. For rechallenge studies, GHP-88309 treatment after the primary infection was discontinued after 9 days, followed by resting of animals until 28 days after the primary infection and intranasal reinfection with 1.5×10^5 $TCID_{50}$ units of recSeV-Fushimi eGFP. A

control group of SeV-naïve mice was infected equally at the time of rechallenge. Mice received no treatment after the second infection, blood was collected on study day 21 and 32 to determine neutralizing antibody titers. For infection with drug-resistant recSeV, animals were infected intranasally as above with the engineered, resistant recombinants or the genetic parent virus, and clinical signs monitored as above. Studies were terminated on day 14 after infection, when no clinical signs were detected and animals infected with the parental recSeV had succumbed to the disease.

Histopathology scoring

Intact lungs were fixed in formalin, embedded in paraffin, sectioned and stained with hematoxylin and eosin. Blinded samples were scored according to the matrix: 0, no change compared to lungs of uninfected mice; 1, minimal signs of immune cell infiltration; 2, mild inflammation and/or immune cell infiltration; 3, moderate inflammation and/or immune cell infiltration, slight thickening of bronchioles; 4, pronounced inflammation and/or immune cell infiltration, moderate thickening of bronchioles and immune infiltration around airways and blood vessels; 5, severe inflammation and/or immune cell infiltration engulfing up to 50% of lung lobe, severe cuffing/thickening of bronchioles and immune infiltration around airways and blood vessels; 6, severe inflammation and/or immune cell infiltration occurring engulfing >50% of lung lobe, severe cuffing/thickening of bronchioles and immune infiltration around airways and blood vessels.

In vivo adaptation of recSeV-eGFP in the presence of GHP-88309

For in vivo adaptation, mice were administered recSeV-Fushimi eGFP or resistant recombinant intranasally at 1.5×10^5 $TCID_{50}$ units in 50 μl of PBS. Prophylactic treatment with GHP-88309 commenced 2 hours before infection administered per oral gavage in a b.i.d. regiment at 50 mg/kg body weight. Infected mice were monitored twice daily for clinical signs (body weight loss, body temperature change, overall composure). Mice were harvested 6.5 days after infection and lung viral titers were determined through $TCID_{50}$ titration of tissue homogenates on Vero-E6 cells. For each recSeV-Fushimi eGFP passaged, a second mouse was infected with 50 μL of passage 1 lung homogenate. Passage 2 mice were harvested 6.5 days after infection and lung viral titers were determined through $TCID_{50}$ titration of tissue homogenates on Vero-E6 cells. RT-PCR was performed on SeV RNA from tissue homogenates. A PCR fragment (L residues 815–1181) was sequenced to identify any potential resistance mutations arising from in vivo passaging of recSeV-eGFP in the presence of GHP-88309.

To determine susceptibility of *in vivo* passaged virus, Vero-E6 cells were infected with harvested SeV-eGFP in 96-well format (5×10^3 cells/well). Infected cells were incubated with increasing concentrations of GHP-88309 (0.13–100 μM). At 80 hours post infection, GFP signal was quantified using a Cytation5 imaging reader (Biotek). Average fluorescent intensity was determined using an area scan function (49 reads/well; excitation/emission = 479/520 nm) using the Gen5 software package (Biotek; v3.05). Infected cells treated with DMSO and cycloheximide were used as negative and positive controls, respectively. Effective concentrations were calculated from dose-response data sets through 4-parameter variable slope regression modeling.

Human 3D-ALI-HBTEC models

3.3×10^4 HBTECs were seeded onto 6.5 mm Costar Transwell Cell Culture Inserts (pore size 0.4 μm) and grown submerged in BronchiaLife cell culture medium to 100% confluency. HBTEC Air-Liquid Interface Differentiation Medium (LifeLine Cell Technology) was then added to the basolateral chamber, and media removed from the apical chamber. Cells were grown at ALI for 21 days, emerging 3D cultures washed every 48 hours to remove excess mucus, and transepithelial/transendothelial resistance (TEER) measured using an EVOM volt/ohm meter coupled with an STX2 electrode (World Precision Instruments). Cultures with resistance ≥700 Ω/cm^2 were used for experimentation. For infection studies, 3D-ALI-HBTECs were apically inoculated with recHPIV3-JS-NanoLuc, HPIV-1–5F6, HPIV3–9R4, or HPIV3–10L3, (5,000 $TCID_{50}$ units/well) for 2 hours and washed thrice with media. Treatment with GHP-88309 or volume-equivalent DMSO was administered from the basal chamber. Released virus was collected from the apical chamber every 24 hours. Treatment efficacy was evaluated by $TCID_{50}$ (recHPIV3-JS-NanoLuc) or $TCID_{50}$-HA (HPIV-1 and HPIV3 clinical isolates) titration of shed virus.

Confocal microscopy

3D cultures were fixed with 4% paraformaldehyde-PBS for 20 minutes followed by permeabilization with 0.5 % TritonX-100-PBS for 2 hours. Nonspecific protein binding sites were blocked with 5% BSA-PBS for 1 hour. HPIV3 was detected using goat anti-HPIV3 (Abcam) followed by anti-goat AF-568 (Thermo Scientific). Muc5AC was detected using mouse anti-Muc5AC (Thermo Scientific). ZO-1 (tight junctions) was detected using mouse anti-ZO-1 (BD Biosciences; 610966). Anti-mouse-FITC secondary antibody (SantaCruz) was used for both Muc5AC and ZO-1 staining. Anti-β-tubulin-647 antibody (Novus Biologicals) was used for detection of β-tubulin. Membranes were placed on glass slides using a mounting medium supplemented with 0.1 mM 4,6-diamidino-2-phenylindole (DAPI; Molecular Probes), covered with a coverslip, and edges sealed with nail polish. A Zeiss LSM 800 confocal microscope coupled with AiryScan module was used for detection, Zeiss Zen Blue software was employed for image analysis.

Chemical synthesis

Synthesis of 2-fluoro-6-(5-isoquinolyl)benzonitrile—2-bromo-6-fluoro-benzonitrile (5.0 gm, 25 mmol), 5-isoquinolylboronic acid (6.0 gm, 35 mmol) and Na_2CO_3 (10.6 gm, 100 mmol) were placed in a 250 ml sealed flask and treated with (2:1)1,4-dioxane:water (90ml). The mixture was purged with argon for 5 min. $Pd(PPh_3)_4$ (2.25gm, 1.94 mmol) was added and purged for another 5 minutes. The reaction mixture was sealed and stirred at 100°C for 3–5 hours. After completion, the reaction mixture was cooled to room temperature, diluted with excess dichloromethane and extracted with water. The aqueous layer was extracted with dichloromethane, the combined organic layers dried over anhydrous Na_2SO_4, filtered, and concentrated under reduced pressure. The crude product was purified by flash column chromatography using dichloromethane and methanol as eluent. Pure product was obtained as colorless solid, yield 77% (4.8 gm).

^{1}H NMR 400 MHz, DMSO-d6, δ 9.44 (1H, s), 8.51 (1H, d, J = 8 Hz), 8.30 (1H, d, J = 8 Hz), 7.96–7.66 (3H, m), 7.68 (1H, t, 8 Hz), 7.50 (1H, d, J = 8 Hz), 7.42 (1H, d, J = 4 Hz);

^{19}F NMR 376 MHz, DMSO-d6 δ −107.10 to −107.14, (1F, m); MS (ES-API) [M+1]+ : 249.0.

Synthesis of 2-fluoro-6-(5-isoquinolyl)benzamide (GHP-88309)—2-fluoro-6-(5-isoquinolyl)benzonitrile (4 gm, 16.1 mmol) was placed in a 100 ml round bottom flask and treated with acetic acid (12 ml, 209 mmol) and conc. H_2SO_4 (6 ml, 112 mmol). The reaction mixture was stirred at 120°C for 2–3 hours. After completion, the reaction mixture was cooled to room temperature and poured on crushed ice and carefully neutralized with aq. NaOH. Aqueous mixture was extracted thrice with ethylacetate, organic layers were combined, dried over anhydrous Na_2SO_4, filtered and concentrated under reduced pressure. The crude product was purified by flash column chromatography using dichloromethane and methanol as eluent. Pure product was obtained as colorless solid, yield 46% (2 gm).

^{1}H NMR 400 MHz, DMSO-d6, δ 9.34 (1H, s), 8.43 (1H, d, J = 4 Hz), 8.14 (1H, d, J = 8 Hz, 2 Hz, 0.8 Hz), 7.87 (1H, bs), 7.70 (2H, m), 7.54 (1H, m), 7.39 (^{3}H, m), 7.16 (1H, dd, J = 8 Hz, 0.8 Hz); ^{19}F NMR 376 MHz, DMSO-d6 δ −116.27 to −116.31, (1F, m); ^{13}C NMR 100 MHz, DMSO-d6, δ 165.81, 158.75 (d, J = 250 Hz), 152.93, 143.54, 138.39, 136.05, 134.18, 131.66, 130.40 (d, J = 9 Hz), 128.68, 128.10, 127.81, 127.61, 127.10, 119.08, 115.55 (d, J = 22 Hz); MS (ES-API) [M+1]+ : 267.0.

Synthesis of chemical analogs—Analogs were generated using the same procedure described for the synthesis of GHP-88309, except GHP-88309–003, GHP-88309–004, GHP-88309–009, GHP-88309–010 and GHP-88309–015. Synthesis of GHP-88309–003 and GHP-88309–004 was achieved by the reaction of 5-bromo-8-nitroquinolone and 8-bromo-4-methoxyquinazoline respectively with (2-cyanophenyl) boronic acid as shown in scheme 1.

In the case of GHP-88309–009 containing acid labile alkyl ether, nitrile to amide conversion was achieved through alternate basic condition[1] **c** as shown in scheme 1. In GHP-88309–010, propargyl group was introduced after boronic acid coupling reaction to avoid potential interference from the alkyne function as shown in scheme 2.

Analogs GHP-88309–010 and GHP-88309–015 were obtained by the conversion of esters to the corresponding amides using condition **b** and **c** respectively as shown in scheme 3.

Analytical data—GHP-88309–001: ^{1}H NMR (400 MHz, Methanol-d_4) δ 8.82 (d, J = 4 Hz, 1H), 8.09–8.04 (m, 2H), 7.77 (dd, J = 8 Hz, 4 Hz, 1H), 7.58–7.51 (m, 2H), 7.44 (dd, J = 4 Hz, 1H), 7.31–7.26 (m, 1H), 7.18 (dd, J = 8 Hz, 1 Hz, 1H); ^{19}F NMR (376 MHz, Methanol-d_4) δ −115.81 (dd, J = 5.6 Hz, J = 9.4 Hz); MS (ES-API) $[M+1]^+$: 267.1.

GHP-88309–002: ^{1}H NMR (400 MHz, Methanol-d_4) δ 8.95 (s, 1H), 8.42 (d, J = 5.8 Hz, 1H), 7.95 (d, J = 9.0 Hz, 1H), 7.84 (d, J = 5.8 Hz, 1H), 7.81–7.77 (m, 1H), 7.63 –7.54 (m, 1H), 7.59– 7.52 (m, 1H), 7.35–7.30 (m, 1H), 7.23 (d, J = 7.6 Hz, 1H); ^{19}F NMR (376 MHz, Methanol-d_4) δ −116.34 (dd, J = 9.3, 5.7 Hz); MS (ES-API) $[M+1]^+$: 267.1.

GHP-88309–003: ^{1}H NMR (400 MHz, Methanol-d_4) δ 9.90 (s, 1H), 8.54 (d, J = 6.0 Hz, 1H), 8.47 (d, J = 7.9 Hz, 1H), 7.84–7.76 (m, 2H), 7.71–7.62 (m, 2H), 7.60 (dd, J = 6.0 Hz, 1.0 Hz, 1H), 7.46–7.42 (m, 1H). MS (ES-API) $[M+1]^+$: 293.9.

GHP-88309–004: ^{1}H NMR (400 MHz, Methanol-d_4) δ 8.63 (s, 1H), 8.23 (dd, J = 8.3 Hz, 1.5 Hz, 1H), 7.86 (dd, J = 7.3 Hz, 1.5 Hz, 1H), 7.73– 7.65 (m, 2H), 7.59 (td, J = 7.5, 1.5 Hz, 1H), 7.52 (td, J = 7.5, 1.4 Hz, 1H), 7.43 (dd, J = 7.5, 1.4 Hz, 1H), 4.21 (s, 3H). MS (ES-API) $[M+1]^+$: 280.0.

GHP-88309–005: ^{1}H NMR (400 MHz, Chloroform-d) δ 9.43 (broad s, 1H), 8.40 (broad s, 1H), 8.13 (d, J = 8 Hz, 1H), 7.88 7.80 (m, 3H), 7.70 (broad s, 1H), 7.65–7.57 (m, 2H). 7.37 (dd, J = 8 Hz, 1 Hz, 1H), 5.66 (broad s, 2H); MS (ES-API) $[M+1]^+$: 249.1.

GHP-88309–006: ^{1}H NMR (400 MHz, Methanol-d_4) δ 9.26 (s, 1H), 8.35 (d, J = 4 Hz, 1H), 8.05 (d, J = 8 Hz, 1H), 7.76–7.68 (m, 3H), 7.25 (dd, J = 8 Hz, 1H), 6.84 (dd, J = 8 Hz, 1 Hz, 1H), 6.63 (dd, J = 8 Hz, 1 Hz, 1H). MS (ES-API) $[M+1]^+$: 264.1.

GHP-88309–007: ^{1}H NMR (400 MHz, DMSO-d_6) δ 9.38 (s, 1H), 8.44 (d, J = 5.9 Hz, 1H), 8.16 (d, J = 7.8 Hz, 1H), 7.89 (s, 1H), 7.77 – 7.66 (m, 2H), 7.48 (d, J = 5.9 Hz, 1H), 7.39 (s, 1H), 7.32 (pseudo t, J = 8.6 Hz, 1H), 7.11 (d, J = 8.4 Hz, 1H), 3.94 (s, 3H). ^{19}F NMR (376 MHz, DMSO-d_6) δ −138.50 (d, J = 8.8 Hz). MS (ES-API) $[M+1]^+$: 297.1.

GHP-88309–008: ^{1}H NMR (400 MHz, Methanol-d_4) δ 9.30 (s, 1H), 8.25 (s, 1H), 8.09 (dd, J = 7 Hz, 2 Hz, 1H), 7.73– 7.68 (m, 2H), 7.60–7.56 (m, 2H), 7.42–7.40 (m, 1H), 7.22 (d, J = 2 Hz, 1H). MS (ES-API) $[M+1]^+$: 283.1.

GHP-88309–009: ^{1}H NMR (400 MHz, Methanol-d_4) δ 9.25 (s, 1H), 8.35 (d, J = 6.1 Hz, 1H), 8.10 (dd, J = 6.4 Hz, 3.1 Hz, 1H), 7.74–7.69 (m, 2H), 7.55 (d, J = 6.1 Hz, 1H), 7.34 (d, J = 8.4 Hz, 1H), 7.30 (d, J = 2.7 Hz, 1H), 7.22 (dd, J = 8.4 Hz, 2.7 Hz, 1H), 4.31 (t, J = 4.8 Hz, 2H), 3.6 (t, J = 4.8 Hz, 2H); MS (ES-API) $[M+1]^+$: 333.9.

GHP-88309–010: ^{1}H NMR (400 MHz, Methanol-d_4) δ 9.26 (s, 1H), 8.34 (d, J = 6.0 Hz, 1H), 8.12 (dd, J = 6.8 Hz, 1H), 7.77–7.68 (m, 3H), 7.64–7.58 (m, 1H), 7.53 (d, J = 6.0 Hz, 1H), 7.40 (d, J = 7.8 Hz, 1H), 4.75 (s, 2H), 4.30 (d, J = 2.4 Hz, 2H), 2.96 (t, J = 2.4 Hz, 1H); MS (ES-API) $[M+1]^+$: 317.1.

GHP-88309–011: 1H NMR (400 MHz, Chloroform-d) δ 9.34 (broad s, 1H), 8.49 (broad s, 1H), 8.09–8.05 (m, 1H), 7.97 (dd, J = 8 Hz, 4 Hz, 1H), 7.73–7.69 (m, 2H), 7.43 (d, J = 8 Hz, 1H), 7.29–7.24 (m, 1H). 7.07 (dd, J = 8 Hz, 1 Hz, 1H); ^{19}F NMR (376 MHz, Chloroform-d) δ −108.31 to −108.36, (m). MS (ES-API) $[M+1]^+$: 267.1.

GHP-88309–012: ^{1}H NMR (400 MHz, Methanol-d_4) δ 9.29 (s, 1H), 8.37 (s, 1H), 8.17 (d, J = 8.1 Hz, 1H), 7.78– 7.74 (m, 1H), 7.69 (d, J = 6.8 Hz, 1H), 7.47–7.44 (m, 1H), 7.33 (d, J = 4.5 Hz, 1H), 7.27–7.23 (m, 1H), 1.87 (s, 3H); ^{19}F NMR (376 MHz, Methanol-d_4) δ −122.16 to −122.20, (m). MS (ES-API) $[M+1]^+$: 281.1.

GHP-88309–013: ^{1}H NMR (400 MHz, Chloroform-d) δ 9.39 (s, 1H), 8.49 (s, 1H), 8.09 (d, J = 8.0 Hz, 1H), 7.75– 7.63 (m, 2H), 7.60–7.50 (m, 2H), 7.29 (dd, J = 7.6 Hz, 0.8 Hz, 1H), 7.19 (dd, J = 7.6 Hz, 0.8 Hz, 1H), 3.42 (s, 3H). ^{19}F NMR (376 MHz, Chloroform-d) δ −113.33 (dd, J = 9.4, 5.2 Hz); MS (ES-API) $[M+1]^+$: 282.1.

GHP-88309–014: ^{1}H NMR (400 MHz, Chloroform-*d*) δ 9.32 (s, 1H), 8.46 (d, *J* = 5.6 Hz, 1H), 8.01 (d, *J* = 8 Hz, 1H), 7.67 (dd, *J* = 8 Hz, 7.2 Hz, 1H), 7.56 (dd, *J* = 7.2 Hz, 1.2 Hz, 1H), 7.32–7.21 (m, 2H), 7.14 (pseudo t, *J* = 8.4 Hz, 1H), 7.02 (d, *J* = 7.6 Hz, 1H), 1.93 (s, 3H); ^{19}F NMR (376 MHz, Chloroform-*d*) δ −115.68 to −115.77 (m). MS (ES-API) $[M+1]^+$: 238.1.

GHP-88309–015: ^{1}H NMR (400 MHz, Methanol-d_4) δ 9.24 (d, *J* = 0.8 Hz, 1H), 8.34 (d, *J* = 6 Hz, 1H), 8.10 (td, *J* = 4.4 Hz, 0.8 Hz, 1H), 7.71 (dd, *J* = 4.8 Hz, 0.8 Hz, 2H), 7.52 (dt, *J* = 6 Hz, 0.8 Hz, 1H), 7.33 (dd, *J* = 8.4 Hz, 0.8 Hz, 1H), 7.25–7.13 (m, 2H), 3.92 (s, 3H). MS (ES-API) $[M+1]^+$: 295.0.

GHP-88309–016: ^{1}H NMR (400 MHz, Methanol-d_4) δ 9.26 (s, 1H), 8.35 (d, *J* = 6.0 Hz, 1H), 8.13 (m, 1H), 7.73 (d, *J* = 4.9 Hz, 2H), 7.52 (dd, *J* = 6 Hz, 1 Hz, 1H), 7.46–7.41 (m, 1H), 7.40–7.37 (m, 1H), 7.35–7.32 (m, 1H); MS (ES-API) $[M+1]^+$: 290.0.

Chemicals

All materials were obtained from commercial suppliers and used without further purification, unless otherwise noted. Dry organic solvents, packaged under nitrogen in septum sealed bottles, were purchased from EMD Millipore and Sigma-Aldrich Co. Reactions were monitored using EMD silica gel 60 F254 TLC plates or using an Agilent 1200 series LCMS system with a diode array detector and an Agilent 6120 quadrupole MS detector. Compound purification was accomplished by liquid chromatography on a Teledyne Isco CombiFlash RF+ flash chromatography system. NMR spectra were recorded on an Agilent NMR spectrometer (400 MHz) at room temperature. Chemical shifts are reported in ppm relative to residual DMSO-d6 signal. The residual shifts were taken as internal references and reported in parts per million (ppm). The screening collection was assembled from commercial libraries (ChemBridge and ChemDiv), both curated against chemical structures with undesirable reactivity, and a proprietary compound collection derived from previous medicinal chemistry optimization campaigns. All compounds were dissolved in DMSO to a concentration of 10 μM and stored at −80°C. To generate a screening set, all compounds were inventoried in MScreen and reformatted into barcoded 384-well format daughter plates using a Nimbus96 liquid handler (Hamilton Robotics). Thirty-two wells on each 384-well plate were reserved for positive and negative (vehicle) controls, arranged in a checkerboard pattern in the two lateral columns on either side.

Database searches

Whole genome sequences from RefSeq, GenBank and other NCBI repositories were retrieved using the portal NCBI Virus (https://www.ncbi.nlm.nih.gov/labs/virus/vssi/#/). Searches were performed for complete L protein sequences using the taxonomy ID of HPIV-1 (NCBI:txid12730, 92 sequences), HPIV-3 (NCBI:txid11216, 392 sequences) and MeV (NCBI:txid11234, 293 sequences).

Statistics and Reproducibility

MScreen, GraphPad Prism, and Excel software packages were used for data analysis. One-way or two-way ANOVA with Dunnett's, Sidak's, or Tukey's multiple comparisons post-

hoc tests without further adjustments were used to evaluate statistical significance when more than two groups were compared or datasets contained two independent variables, respectively. The specific statistical test applied to individual studies is specified in figure legends. Source Data file (Plemper_SourceData_Statistics) summarizes the test statistic (effect size, degrees of freedom, P values) for every statistical analysis conducted in this study. Appropriateness of samples sizes was determined through Resource Equation and Power analyses as specified in Source Data file (Plemper_SourceData_Statistics). Effect sizes between groups in ANOVAs were calculated as $\eta^2 = (SS_{effect}) / (SS_{total})$ [one-way ANOVA] and $\omega^2 = (SS_{effect} - (df_{effect})(MS_{error})) / MS_{error} + SS_{total}$ [two-way ANOVA]. Survival data were analyzed using a time-to-event log-rank (Mantel-Cox) test. To determine antiviral potency and cytotoxicity, effective concentrations were calculated from dose-response data sets through 4-parameter variable slope regression modeling; values are expressed with 95% confidence intervals (CIs). Biological repeat refers to measurements taken from distinct samples, and results obtained for each individual biological repeat are shown in the figures along with the exact size (n number) of biologically independent samples, animals, or independent experiments. Measure of center (connecting lines and columns) are means throughout, with the exception of figures 5a–e and 6i, which show medians as specified in figure legends. Error bars represent standard deviations (SD) throughout. For all experiments, the statistical significance level α was set to <0.05, exact P values are shown in individual graphs wherever possible.

Ethics statement

All animal studies were performed following the Guide for the Care and Use of Laboratory Animals. All experiments were approved by the Institutional Animal Care and Use Committee of Georgia State University (protocol AL17019) and conducted in compliance with the Association for the Accreditation of Laboratory Animal Care guidelines, National Institutes of Health regulations, Georgia State University policy, and local, state, and federal laws. Mice were anesthetized with isoflurane and euthanized using carbon dioxide.

Human subjects

Normal primary human bronchial tracheal epithelial cells (HBTECs) used in this project were sourced from a commercial provider, LifeLine Cell Technology (https://www.lifelinecelltech.com/human-cell-systems/management/). These specimens were obtained by the vendor under informed consent and adhere to the Declaration of Helsinki, The Human Tissue Act (UK), CFR Title 21, and HIPAA regulations as specified in https://www.lifelinecelltech.com/technical-support/ethics/. All regulatory approval lies with the vendor. LifeLine Cell Technology was not involved in study design and had no role, active or advisory, in the project, which includes no involvement in execution of experiments and interpretation of study results. To protect privacy of donors and tissue suppliers, LifeLine Cell Technology does not provide copies of donor records or tissue source agreements. The vendor holds donor consent and legal authorizations that give permission for all research use. These consent and authorization documents do not identify specific types of research testing. If used for research purposes only, the donor consent applies.

Data availability statement

Raw data, original, and/or replicates for all biological experiments in main and Extended Data figures and Supplementary Information is provided in the Source Data files associated with the individual figures. Confocal microscopy and histology raw data files have been deposited at figshare (access links are specified in figure legends). HPIV3 whole genome sequencing data of the DMSO treated and GHP-88309 treated passages are available in NCBI BioProject PRJNA561835. SeV next-generation sequencing data are available in NCBI GEO ID GSE140376. HTS raw data is available from the corresponding author upon request. However, no chemical structure information concerning the composition of screening libraries and unsuccessful hit candidates will be provided.

Code availability statement

The open source MScreen package is available from the Center for Chemical Genomics at the University of Michigan. The Longitudinal Analysis of Viral Alleles (LAVA) package is available at https://github.com/michellejlin/lava. Chemical filter algorithms used are available at http://swissadme.ch and http://pasilla.health.unm.edu/tomcat/badapple/badapple. Homology modeling software is available from the Swiss Homology modeling server at http://swissmodel.expasy.org. Power analysis software used is available at http://www.psychologie.hhu.de/arbeitsgruppen/allgemeine-psychologie-und-arbeitspsychologie/gpower.html. All other software solutions employed are commercially available from the developing houses.

Extended Data

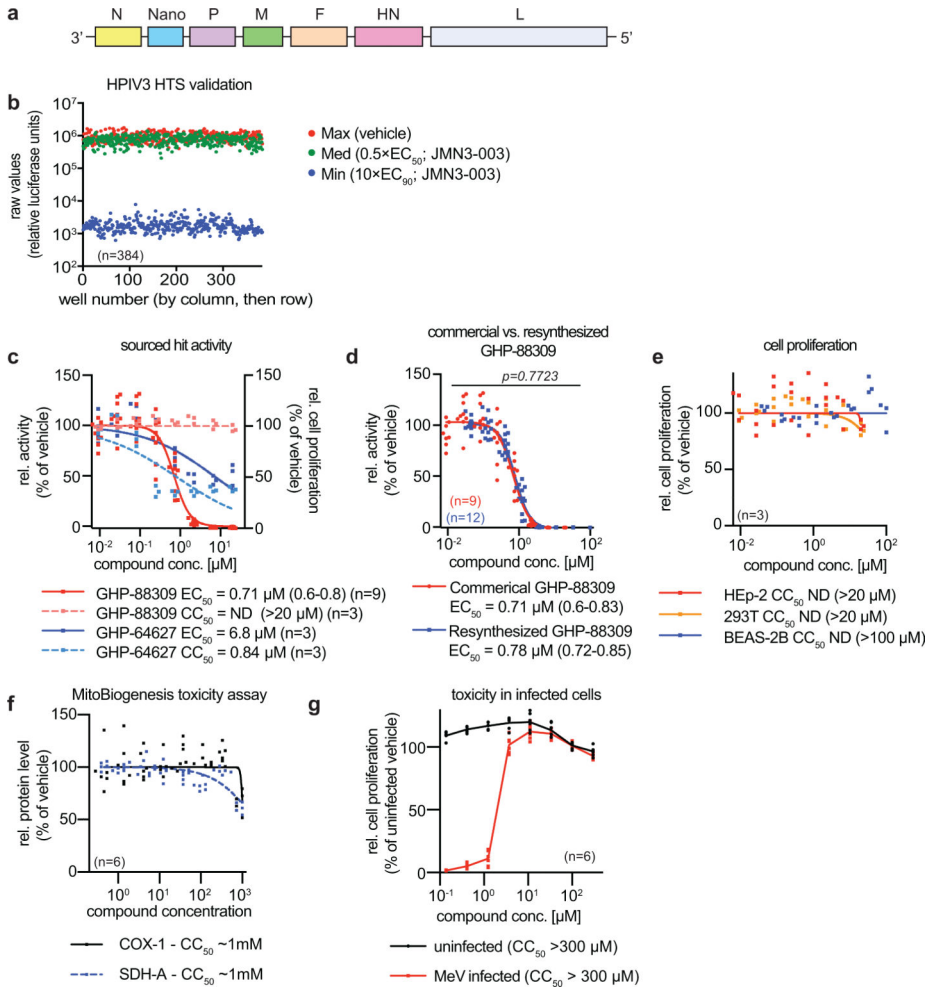

Extended Data Fig. 1: Anti-HPIV3 HTS hit identification.

a, Schematic of genome organization of recHPIV3-JS-NanoLuc. **b**, Validation of automated HTS protocol in 384-well format, using recHPIV3-JS-NanoLuc as detection agent. Three 384-well assay validation plates featuring alternating columns containing vehicle (Max) or the broad-spectrum host-directed inhibitor JMN3–003 in intermediate (0.5 × EC_{50}; Med) or sterilizing (10 × EC_{50}; Min) concentrations. On each validation plate, control columns were arranged in different order. Results for one plate are shown, performance parameters for all three plates and statistical assessments are provided in Supplementary Table 8. **c**, Dose-response antiviral activity and cytotoxicity tests with sourced hit candidates GHP-88309 and GHP-64627. **d**, Comparison of antiviral activity of commercially sourced and resynthesized GHP-88309. No significant differences were noted (P=0.7723). Statistical analysis through the extra sum-of-squares F test. **e,** Effect of GHP-88309 on cell proliferation of different immortalized cell lines. No toxicity was detectable in the concentration range tested (up to 100 μM). **f)** Effect of GHP-88309 on metabolic activity of primary human BTECs. Cytotoxicity was assessed by measuring COX-1 protein levels relative to vehicle treated HBTECs. Effects of compound incubation was assessed in a dose-response format with the

highest concentration equal to 1000 μM. Mitochondrial toxicity was tested in parallel after by measuring SDH-A protein levels relative to vehicle treated HBTECs. Protein levels were measured after 72-hour incubation with GHP-88309. **g**, MeV infected cells (MOI 0.5 $TCID_{50}$ units/cell) were incubated with GHP-88309 at increasing compound concentrations for 48 hours. Cell viability was measured and normalized to uninfected, vehicle treated cells using PrestoBlue assay. GHP-88309 exhibited no toxicity at concentrations up 300 μM. In (c-g), symbols represent biological repeats, lines are derived from 4-parameter variable slope regression modeling (c-g). Where applicable, active (EC_{50}) and cytotoxic (CC_{50}) concentrations are shown with 95% confidence intervals (CIs) in parentheses.

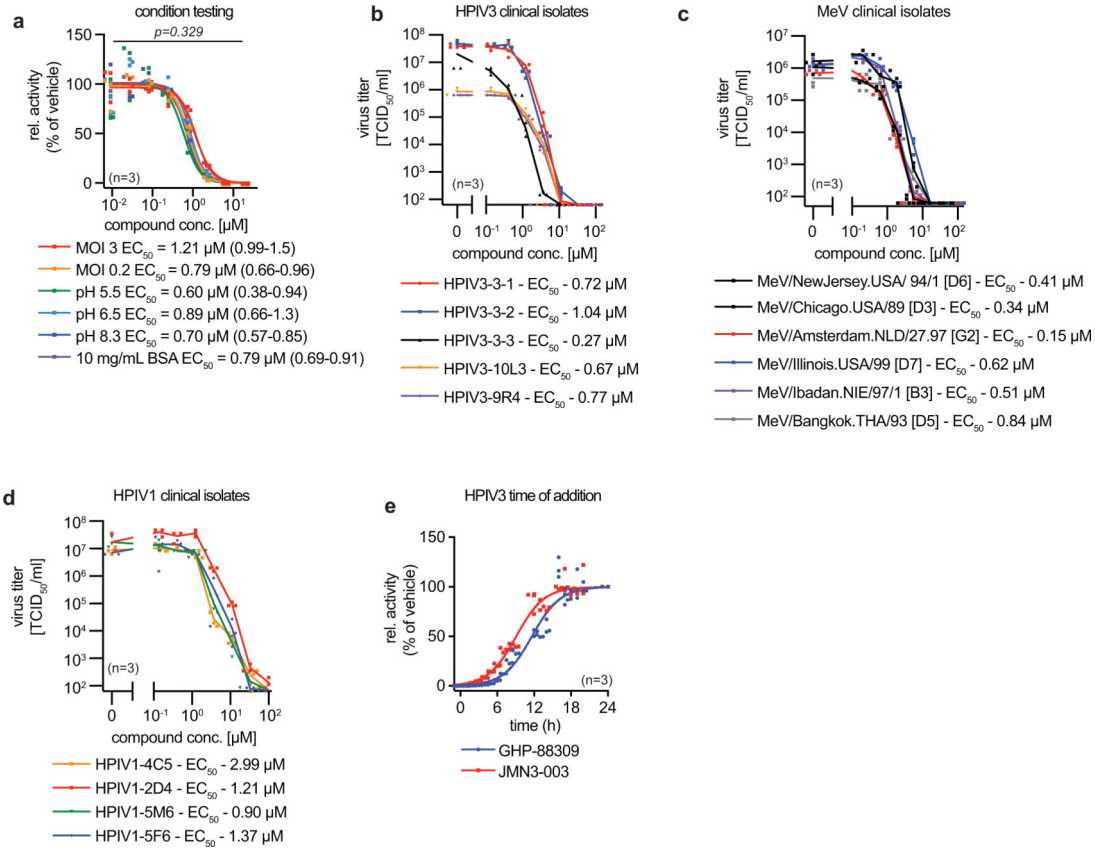

Extended Data Fig. 2: GHP-88309 hit validation.

a, Antiviral activity of GHP-88309 determined under different conditions (after infection at high MOI; at different media pH; in the presence of BSA). No significant differences were noted (P=0.329). Statistical analysis through the extra sum-of-squares F test. Symbols represent biological repeats, lines connect data means. **b-d**, Efficacy of GHP-88309 against different clinical isolates of HPIV3 (10L3 (KY973583), 9R4 (KY674929), 3–1, 3–2, and 3–3) (b), MeV (c), and HPIV1 (4C5, 2D4 (MF554715.1), 5M6 (MF554714.1), and 5F6) (d). Progeny virus yields from dose-response tests were determined through $TCID_{50}$ titration. GHP-88309 consistently inhibited all target virus strains with low-micromolar to submicromolar potency; EC_{50} concentrations are shown. **e,** HPIV3 ToA studies. GHP-88309 was added at the specified time points after infection at 20 μM. The host-directed polymerase inhibitor JMN3–003 was included for reference.

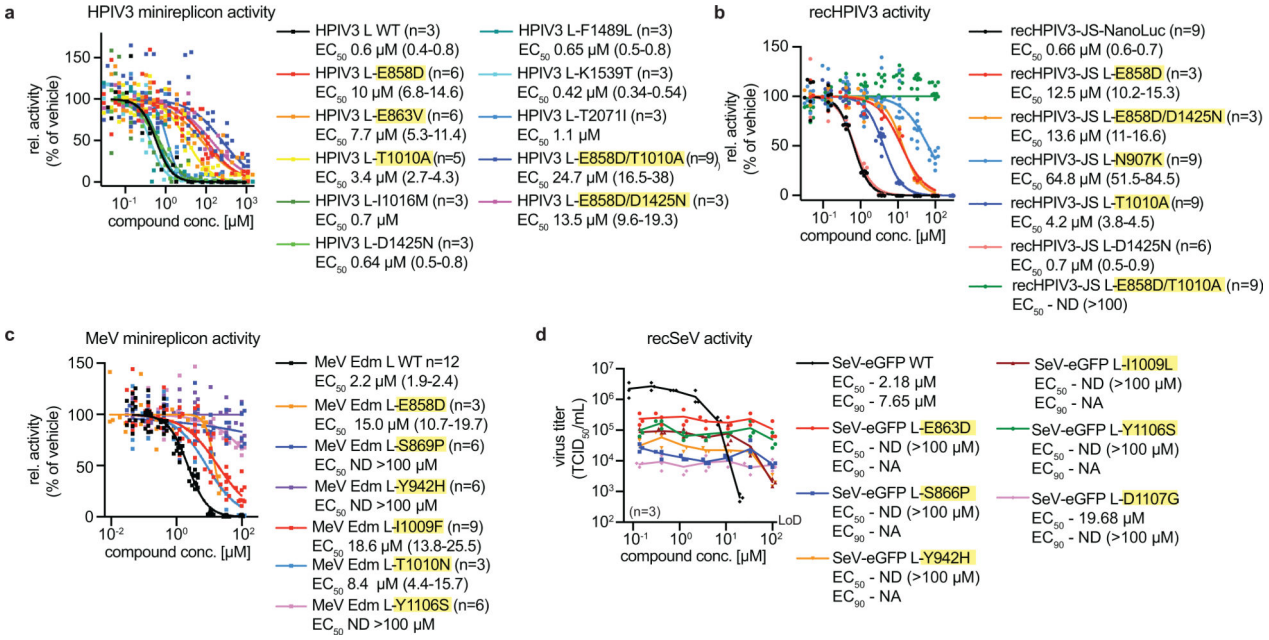

Extended Data Fig. 3: Characterization of viral resistance mutations to GHP-88309.

a, All candidate resistance mutations emerging from adaptation of HPIV3 and two engineered combinations thereof were rebuilt and tested in an HPIV minigenome assay of RdRP activity in the presence of GHP-88309. **b,** Mutations from (a) that were rebuilt in recHPIV3-JS-NanoLuc and tested against GHP-88309 in reporter dose-response assays. **c,** Candidate mutations emerging from MeV adaptation were rebuilt and tested in an MeV minigenome assay of RdRP activity. **d,** All candidate resistance mutations emerging from SeV adaptation were rebuilt in recSeV and tested against the resulting recSeVs in virus yield-based dose-response assays. In (a-d), symbols represent biological repeats, lines are derived from 4-parameter variable slope regression modeling, and active concentrations (EC_{50} and EC_{90} if applicable) are shown with 95% CIs. Yellow highlights denote experimentally confirmed resistance mutations.

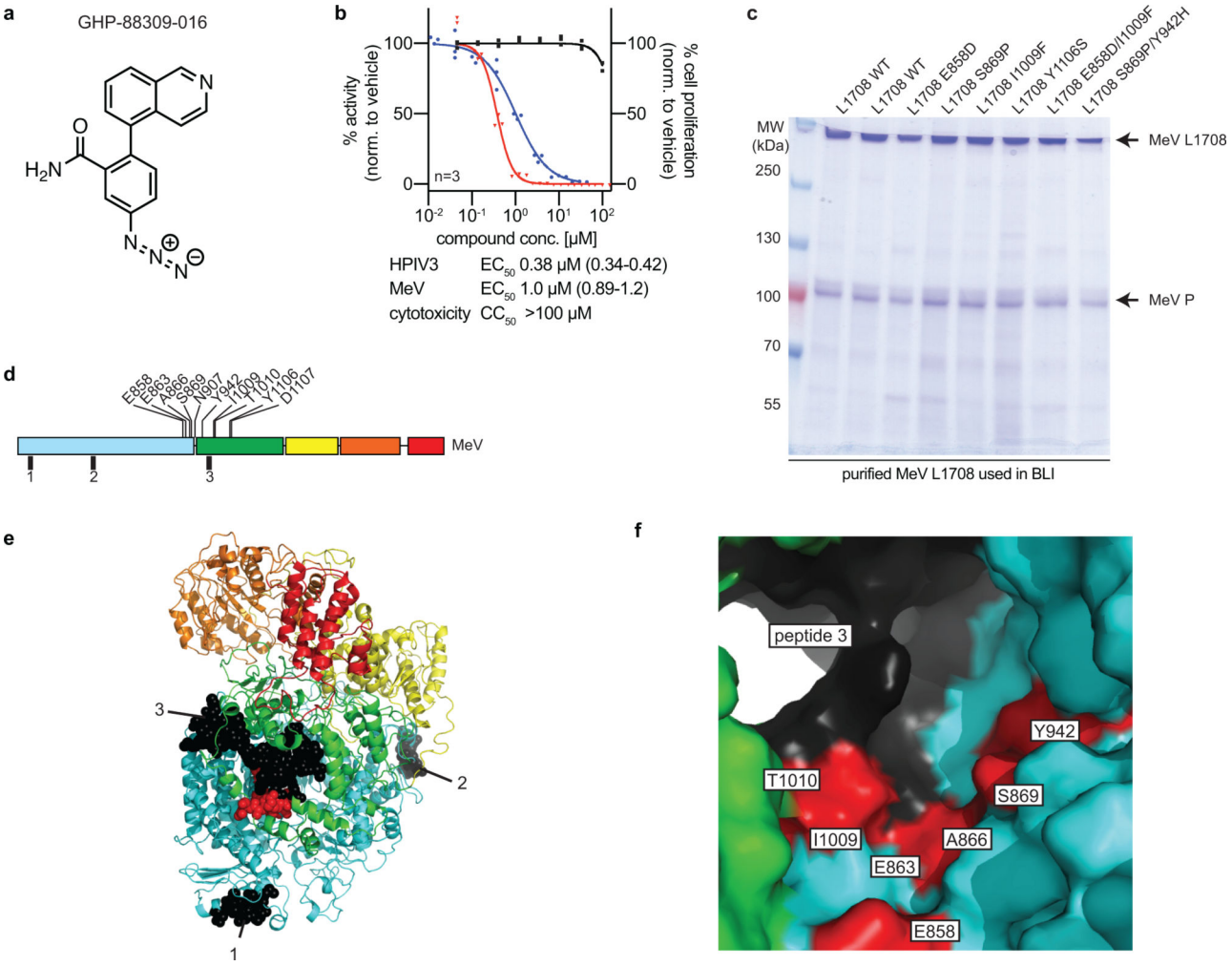

Extended Data Fig. 4: GHP-88309–016 target mapping through photoaffinity labeling.

a, Structure of GHP-88309–016. **b**, GHP-88309–016 is bioactive, potently inhibiting MeV and HPIV3 replication without appreciable cytotoxicity (n=3). EC_{50} values from 4-parameter variable slope regression models are shown with 95% CIs. **c,** SDS-PAGE fractionation of purified MeV L_{1708} constructs used in UV crosslinking and BLI studies on 7.5% gels, followed by Coomassie blue staining. Polymerase complexes were purified once in sufficient quantity to meet the needs of the project. **d**, 2D-schematic of the MeV L protein with locations of known resistance mutations (top) and peptides identified by photoaffinity labeling (bottom; black bars). Cyan, green, yellow, orange, and red depict the RdRP, capping, connector, MTase, and C-terminal domains. **e**, Homology model of MeV L showing the locations of the peptides crosslinked to GHP-88309–016 (black spheres). Confirmed GHP-88309 resistance sites are shown in red. Peptides 1 and 2 are located on the exterior of the polymerase. **f**, Only residues of peptide 3 (black) are exposed to the interior channels of the polymerase in proximity of the resistance sites (red). The homology model was based on the coordinates reported for HPIV5 L (PDB: 6v85).

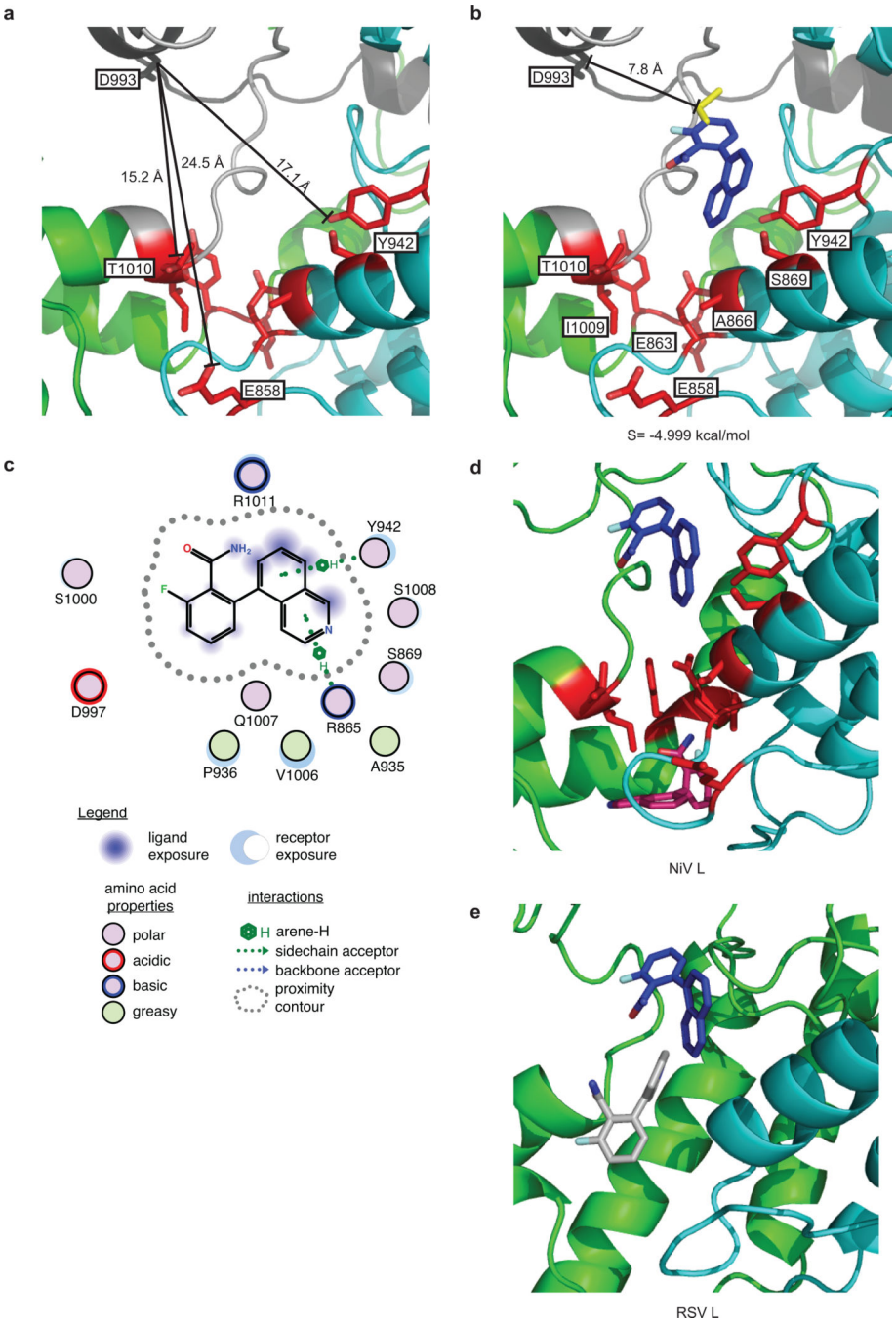

Extended Data Fig. 5:

In silico docking of GHP-88309.

a, Ribbon representation of the MeV L internal channel, showing distances between confirmed resistance sites (red) and the nearest residue in photoaffinity labeled peptide 3 (D993; black). Polymerase domain color-coding as in Fig. 2a. **b,** Docking of GHP-88309 (blue sticks) and GHP-88309–016 (yellow sticks) into the MeV L model, using D993 and confirmed resistance hot-spots as target site guides. The top-scoring pose is conserved between GHP-88309 and GHP-88309–016, and positions the between capping and RdRP

domains. The aryl-azide moiety is located approximately 7.8 Å from residue D993 in peptide 3. Numbers denote predicted free energy associated with this docking pose. **c**, 2D-diagram of predicted top-scoring ligand interaction generated with MOE. Predicted are hydrogen bond interactions between the isoquinoline ring of GHP-88309 and residues Y942 and R865. The benzamide moiety is posited between residues Q1007 and R1011, thus overall linking RdRP and capping domains. **d-e,** Application of the equivalent *in silico* docking approach as in (b) to NiV (d) and RSV L (e). Top scoring poses in NiV (pink sticks) and RSV (white sticks) L are distinct from that in MeV L (superimposed as blue sticks). Known resistance mutations are colored red (a-b, d, e). NiV homology model is based on HPIV5 L (PDB: 6v85); RSV L is native (PDB: 6pzk).

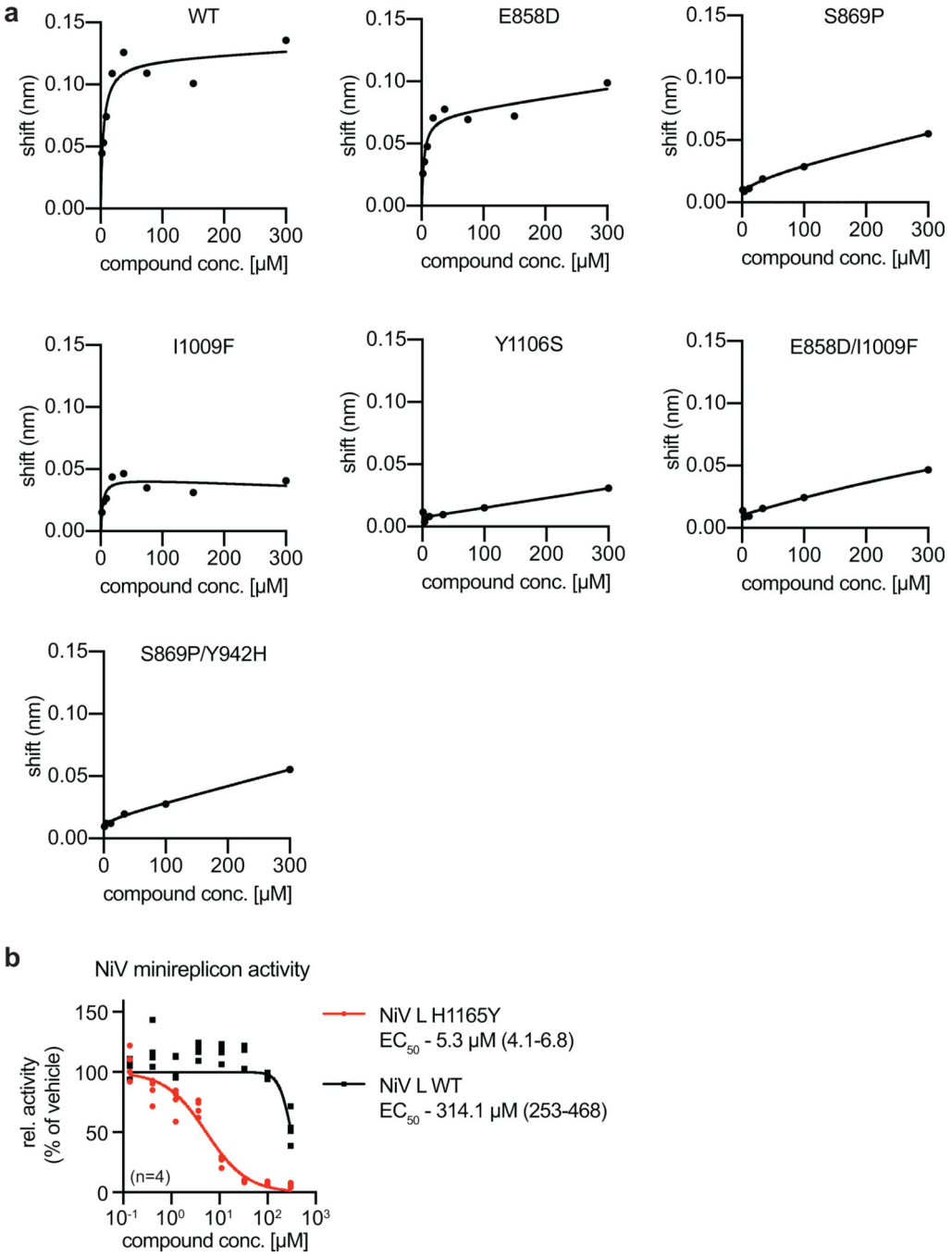

Extended Data Fig. 6: Steady-state analyses of BLI binding saturation and sensitization of NiV L to GHP-88309.

a, Concentration-dependent steady-state BLI sensor response signals were plotted for the different MeV L_{1708} samples (standard (WT) or carrying resistance mutations as indicated) to probe whether saturation of binding was reached. **b,** NiV minigenome assays to test inhibitory activity of GHP-88309 against standard NiV RdRP and NiV RdRP harboring an L_{H1165Y} point mutation. Symbols represent biological repeats, lines are derived from 4-

parameter variable slope regression modeling, and active concentrations (EC_{50} and EC_{90} if applicable) are shown with 95% CIs.

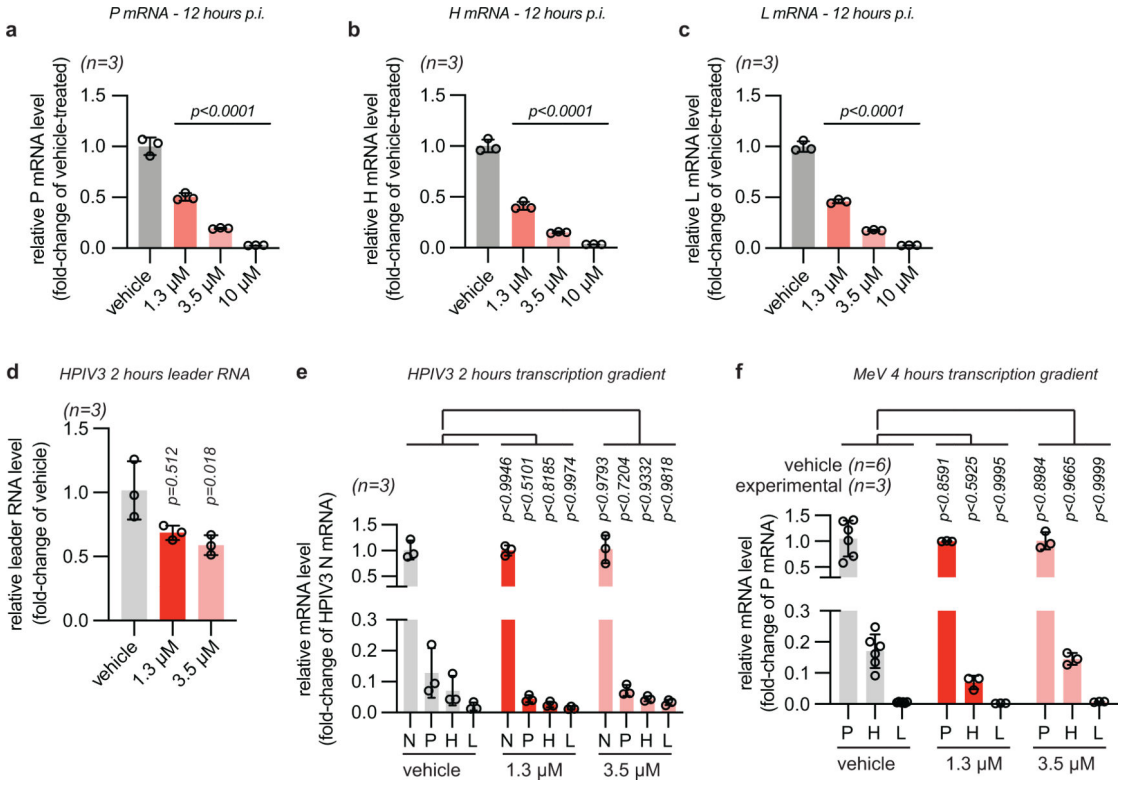

Extended Data Fig. 7: Effect of GHP-88309 treatment on HPIV3 and MeV primary transcription.

a-c, GHP-88309 significantly reduced levels of MeV P (a), H (b), and L (c) mRNA transcripts at 12 hours after infection. **d**, GHP-88309 significantly reduced the synthesis of HPIV3 Le RNA 2 hours after infection. **e-f**, GHP-88309 did not significantly alter the HPIV3 (e; 2 hours after infection) and MeV (f; 4 hours after infection) primary mRNA transcription gradients. Values represent relative changes compared to vehicle treated samples (a-d) or relative changes compared to HPIV3 N (e) or MeV P (f) mRNA levels. Experiments were conducted in at least three biological repeats, determined in duplicate each. In (a-f), symbols represent individual biological repeats, columns denote means, and error bars represent SD. Statistical significance was determined by one-way ANOVA (a-d) or two-way ANOVA (e-f) using Dunnett's multiple comparison post-hoc test (two-sided).

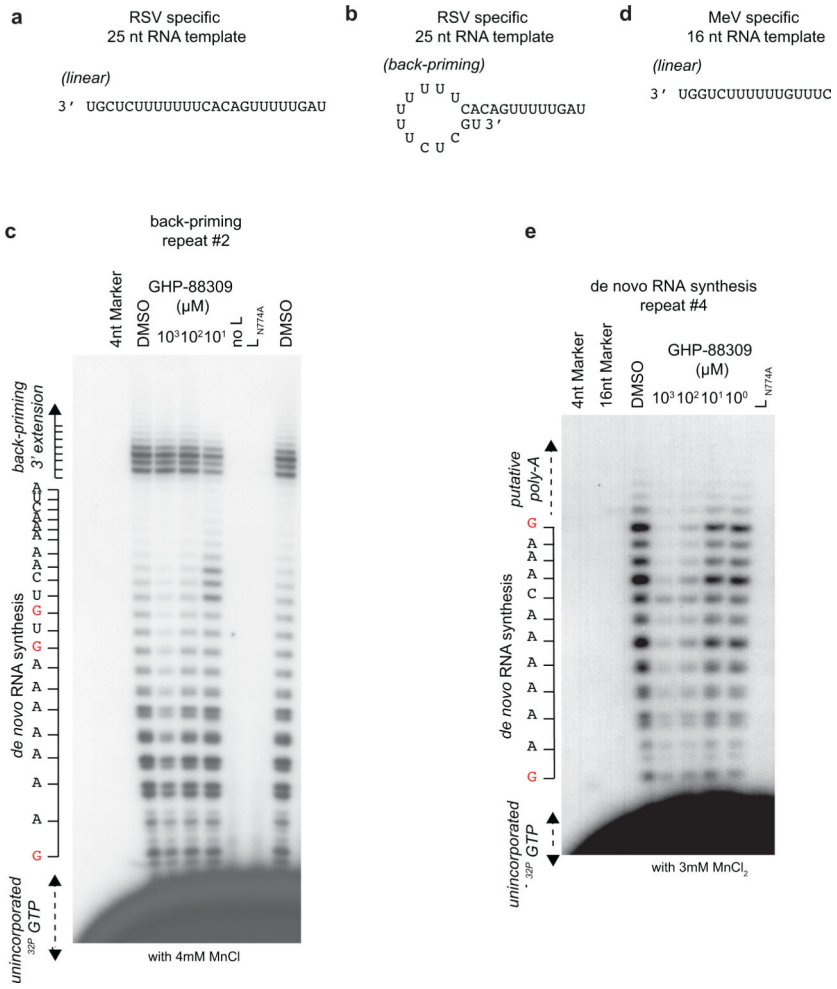

Extended Data Fig. 8: GHP-88309 inhibits *de novo* initiation of RNA synthesis at the promoter.

a-b, RSV-derived RNA template (a) that was used in Fig. 2j and is capable of back-priming depicted in (b). **c,** Repeat result of the MeV RdRP assay with the RSV-derived template shown in Fig. 2; originals are provided in Source Data file (Plemper_SourceData_Fig2_Originals_Repeats.pdf). **d**, MeV-derived RNA template, incapable of back-priming. **e,** MeV RdRP assay with the MeV-derived template shown (d). The experiment was performed three times with similar results. Originals and repeats are provided in (Plemper_SourceData_ED_Fig8_Originals_Repeats.pdf). Higher molecular weight material in (e) likely represents poly-adenylation consistent with previous results obtained with a similar template and NiV polymerase complexes[48].

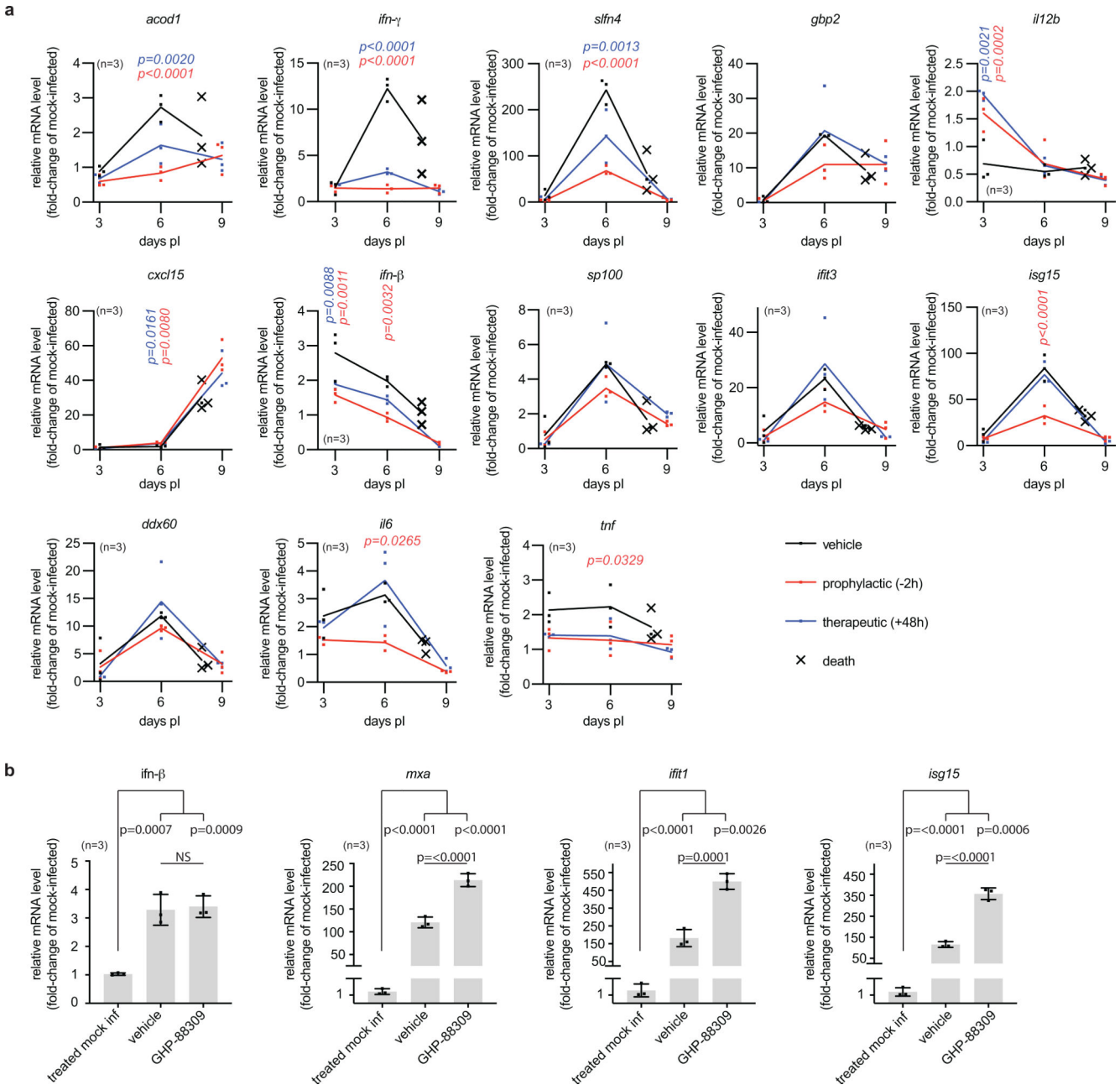

Extended Data Fig. 9: Effect of GHP-88309 treatment on host innate immune response activation.

Individual measurement of data summarized in figure 5h are shown. **a,** Relative expression of genes involved in innate host antiviral response pathways, determined through qRT-PCR three, six, and nine days after SeV infection of mice. Results are shown for vehicle treated (black), prophylactically treated (2 hours before infection; red), and therapeutically treated (48 hours after infection; blue) mice, all normalized to mock-infected and untreated reference animals (n=3 in all groups). Statistical analysis with two-way ANOVA and Tukey's multiple comparison post-hoc test. **b,** Relative induction of type-1 IFN and interferon stimulated genes in undifferentiated HBTECs after HPIV3 infection and treatment

with 6 μM GHP-88309. Cells were mock infected and exposed to GHP-88309 (treated mock inf), HPIV3 infected and vehicle-treated (vehicle), or HPIV3 infected and GHP-88309 treated starting 2 hours before infection. All results are expressed relative to untreated, mock-infected cells. Symbols represent measurements from individual mice (a) or individual biological repeats (b), columns in (b) show data means (n=3) throughout, error bars represent SD. Statistical analysis with one-way ANOVA and Tukey's multiple comparison post-hoc test; NS, not significant.

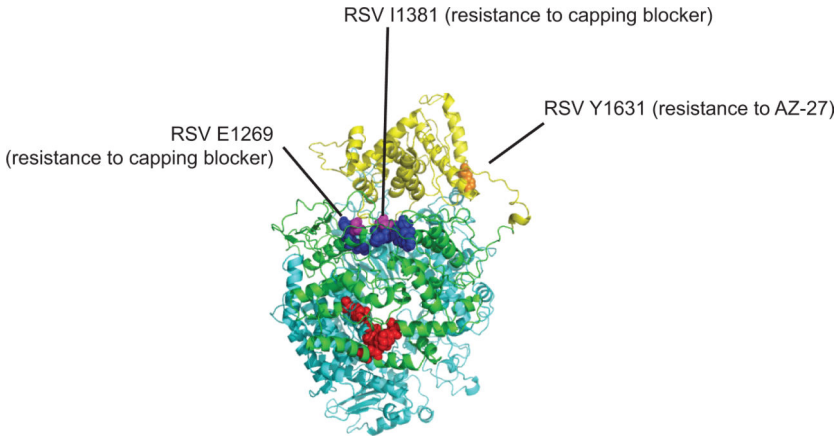

Extended Data Fig. 10: Mapping of RSV L capping blocker and AZ-27 resistance hotspots.
Analogous positions of resistance mutations against the RSV L capping inhibitor compound C (E1269D and I1381S; magenta spheres) and initiation blocker AZ-27 (Y1631; orange spheres) are projected onto an HPIV3 L homology model when locatable. Resistance mutations against the capping inhibitor are proximal to conserved PRNTase motifs (blue spheres) and distal to GHP-88309 resistance mutations (red spheres). The RdRP, connector, and capping domains are color-coded as in Fig. 2a. The HPIV3 L homology model is based on the coordinates reported for HPIV5 L (PDB: 6v85).

Supplementary Material

Refer to Web version on PubMed Central for supplementary material.

Acknowledgements

We thank MT Saindaine and MA Lockwood for chemical synthesis, J Wolf for assistance with molecular biology, H-Y Tang and the Wistar Institute Proteomics and Metabolomics Facility for assistance with proteomics analysis, BR tenOever for NGS support, KK Conzelmann for the BSR-T7/5 stable cell line, and RT Jacob for IT support. The MScreen software package was kindly provided by the Center for Chemical Genomics of the University of Michigan under a license agreement by the University of Michigan Office of Technology Transfer; JChem was used for structure database management, search, and prediction (JChem 6.2, 2014, ChemAxon); and Marvin was employed for drawing, displaying, and characterizing chemical structures, substructures, and reactions (Marvin 14.9.22.0, 2014, ChemAxon). This work was supported, in part, by Public Health Service grants AI071002 (to RKP) and HD079327 (to RKP), from the NIH/NIAID and NIH/NICHD, respectively. The funders had no role in study design, data collection and interpretation, or the decision to submit the work for publication.

References

1. Griffin DE The Immune Response in Measles: Virus Control, Clearance and Protective Immunity. Viruses 8, doi:10.3390/v8100282 (2016).

2. Schomacker H, Schaap-Nutt A, Collins PL & Schmidt AC Pathogenesis of acute respiratory illness caused by human parainfluenza viruses. Curr. Opin. Virol. 2, 294–299, doi:10.1016/j.coviro.2012.02.001 (2012). [PubMed: 22709516]

3. Krumm SA et al. An orally available, small-molecule polymerase inhibitor shows efficacy against a lethal morbillivirus infection in a large animal model. Sci. Transl. Med. 6, 232ra252, doi:10.1126/scitranslmed.3008517 (2014).

4. Unicef. Immunization.. Unicef data. (2018.).

5. Digital N Childhood vaccination coverage statistics—England 2017–18.. (2018.).

6. Gahr P et al. An outbreak of measles in an undervaccinated community. Pediatrics 134, e220–228, doi:10.1542/peds.2013-4260 (2014). [PubMed: 24913790]

7. WHO. Measles Fact Sheet. (2019).

8. Tong AS et al. Paramyxovirus Infection: Mortality and Morbidity in a Pediatric Intensive Care Unit. J Trop Pediatr 62, 352–360, doi:10.1093/tropej/fmw016 (2016). [PubMed: 27037248]

9. Laventhal N, Tarini BA & Lantos J Ethical issues in neonatal and pediatric clinical trials. Pediatr Clin North Am 59, 1205–1220, doi:10.1016/j.pcl.2012.07.007 (2012). [PubMed: 23036252]

10. DeVincenzo JP et al. Viral load drives disease in humans experimentally infected with respiratory syncytial virus. Am. J. Respir. Crit. Care Med. 182, 1305–1314, doi:10.1164/rccm.201002-0221OC (2010). [PubMed: 20622030]

11. Cockerill GS, Good JAD & Mathews N State of the Art in Respiratory Syncytial Virus Drug Discovery and Development. J. Med. Chem. 62, 3206–3227, doi:10.1021/acs.jmedchem.8b01361 (2019). [PubMed: 30411898]

12. Hanfelt-Goade D et al. A Phase 2b, Randomized, Double-Blind, Placebo-Controlled Trial of Presatovir (GS-5806), a Novel Oral RSV Fusion Inhibitor, for the Treatment of Respiratory Syncytial Virus (RSV) in Hospitalized Adults. NEW INSIGHTS IN ACUTE PULMONARY INFECTIONS C17.

13. Gottlieb J et al. A Phase 2b Randomized Controlled Trial of Presatovir, an Oral RSV Fusion Inhibitor, for the Treatment of Respiratory Syncytial Virus (RSV) in Lung Transplant (LT) Recipients. The Journal of Heart and Lung Transplantation 37.

14. Rothan HA et al. Small molecule grp94 inhibitors block dengue and Zika virus replication. Antiviral Res. 171, 104590, doi:10.1016/j.antiviral.2019.104590 (2019). [PubMed: 31421166]

15. Ma C, Li F, Musharrafieh RG & Wang J Discovery of cyclosporine A and its analogs as broad-spectrum anti-influenza drugs with a high in vitro genetic barrier of drug resistance. Antiviral Res. 133, 62–72, doi:10.1016/j.antiviral.2016.07.019 (2016). [PubMed: 27478032]

16. Spickler C et al. Phosphatidylinositol 4-kinase III beta is essential for replication of human rhinovirus and its inhibition causes a lethal phenotype in vivo. Antimicrob. Agents Chemother. 57, 3358–3368, doi:10.1128/AAC.00303-13 (2013). [PubMed: 23650168]

17. Supko JG, Hickman RL, Grever MR & Malspeis L Preclinical pharmacologic evaluation of geldanamycin as an antitumor agent. Cancer Chemother Pharmacol 36, 305–315, doi:10.1007/BF00689048 (1995). [PubMed: 7628050]

18. Adcock RS, Chu YK, Golden JE & Chung DH Evaluation of anti-Zika virus activities of broad-spectrum antivirals and NIH clinical collection compounds using a cell-based, high-throughput screen assay. Antiviral Res. 138, 47–56, doi:10.1016/j.antiviral.2016.11.018 (2017). [PubMed: 27919709]

19. Enkirch T et al. Identification and in vivo Efficacy Assessment of Approved Orally Bioavailable Human Host Protein-Targeting Drugs With Broad Anti-influenza A Activity. Front. Immunol. 10, 1097, doi:10.3389/fimmu.2019.01097 (2019). [PubMed: 31244822]

20. Brown NA Progress towards improving antiviral therapy for hepatitis C with hepatitis C virus polymerase inhibitors. Part I: Nucleoside analogues. Expert Opin Investig Drugs 18, 709–725, doi:10.1517/13543780902854194 (2009).

21. Johnson EM Developmental toxicity and safety evaluations of ribavirin. Pediatr. Infect. Dis. J. 9, S85–87 (1990). [PubMed: 2235213]

22. Gentile I, Buonomo AR, Zappulo E & Borgia G Discontinued drugs in 2012 – 2013: hepatitis C virus infection. Expert Opin Investig Drugs 24, 239–251, doi:10.1517/13543784.2015.982274 (2015).

23. McKenzie R et al. Hepatic failure and lactic acidosis due to fialuridine (FIAU), an investigational nucleoside analogue for chronic hepatitis B. N Engl J Med 333, 1099–1105, doi:10.1056/NEJM199510263331702 (1995). [PubMed: 7565947]
24. Nichols WG, Corey L, Gooley T, Davis C & Boeckh M Parainfluenza virus infections after hematopoietic stem cell transplantation: risk factors, response to antiviral therapy, and effect on transplant outcome. Blood 98, 573–578, doi:10.1182/blood.v98.3.573 (2001). [PubMed: 11468152]
25. Peck AJ et al. Respiratory virus infection among hematopoietic cell transplant recipients: evidence for asymptomatic parainfluenza virus infection. Blood 110, 1681–1688, doi:10.1182/blood-2006-12-060343 (2007). [PubMed: 17502457]
26. Lee MS, Walker RE & Mendelman PM Medical burden of respiratory syncytial virus and parainfluenza virus type 3 infection among US children. Implications for design of vaccine trials. Hum Vaccin 1, 6–11, doi:10.4161/hv.1.1.1424 (2005). [PubMed: 17038832]
27. Abedi GR et al. Estimates of Parainfluenza Virus-Associated Hospitalizations and Cost Among Children Aged Less Than 5 Years in the United States, 1998–2010. J Pediatric Infect Dis Soc 5, 7–13, doi:10.1093/jpids/piu047 (2016). [PubMed: 26908486]
28. Plemper RK & Cox RM Biology must develop herd immunity against bad-actor molecules. PLoS Pathog. 14, e1007038, doi:10.1371/journal.ppat.1007038 (2018). [PubMed: 29953540]
29. Auld DS, Inglese J & Dahlin JL in Assay Guidance Manual (eds Sittampalam GS et al.) (2004).
30. Coan KE & Shoichet BK Stability and equilibria of promiscuous aggregates in high protein milieus. Mol Biosyst 3, 208–213, doi:10.1039/b616314a (2007). [PubMed: 17308667]
31. Habig M et al. Efficient elimination of nonstoichiometric enzyme inhibitors from HTS hit lists. J Biomol Screen 14, 679–689, doi:10.1177/1087057109336586 (2009). [PubMed: 19470716]
32. Iketani S et al. Viral Entry Properties Required for Fitness in Humans Are Lost through Rapid Genomic Change during Viral Isolation. MBio 9, doi:10.1128/mBio.00898-18 (2018).
33. Plemper RK et al. Design of a small-molecule entry inhibitor with activity against primary measles virus strains. Antimicrob. Agents Chemother. 49, 3755–3761, doi:49/9/3755 [pii] 10.1128/AAC.49.9.3755–3761.2005 (2005). [PubMed: 16127050]
34. Krumm SA et al. Potent host-directed small-molecule inhibitors of myxovirus RNA-dependent RNA-polymerases. PLoS One 6, e20069, doi:10.1371/journal.pone.0020069 (2011). [PubMed: 21603574]
35. Yin HS, Paterson RG, Wen X, Lamb RA & Jardetzky TS Structure of the uncleaved ectodomain of the paramyxovirus (hPIV3) fusion protein. Proc. Natl. Acad. Sci. U. S. A. 102, 9288–9293 (2005). [PubMed: 15964978]
36. Moscona A Entry of parainfluenza virus into cells as a target for interrupting childhood respiratory disease. J Clin Invest 115, 1688–1698, doi:10.1172/JCI25669 (2005). [PubMed: 16007245]
37. Palermo LM et al. Human parainfluenza virus infection of the airway epithelium: viral hemagglutinin-neuraminidase regulates fusion protein activation and modulates infectivity. J. Virol. 83, 6900–6908, doi:10.1128/JVI.00475-09 (2009). [PubMed: 19386708]
38. Porotto M, Palmer SG, Palermo LM & Moscona A Mechanism of fusion triggering by human parainfluenza virus type III: communication between viral glycoproteins during entry. J. Biol. Chem. 287, 778–793, doi:10.1074/jbc.M111.298059 (2012). [PubMed: 22110138]
39. Abdella R, Aggarwal M, Okura T, Lamb RA & He Y Structure of a paramyxovirus polymerase complex reveals a unique methyltransferase-CTD conformation. Proc. Natl. Acad. Sci. U. S. A. 117, 4931–4941, doi:10.1073/pnas.1919837117 (2020). [PubMed: 32075920]
40. Mackinnon AL & Taunton J Target Identification by Diazirine Photo-Cross-linking and Click Chemistry. Curr. Protoc. Chem. Biol. 1, 55–73, doi:10.1002/9780470559277.ch090167 (2009). [PubMed: 23667793]
41. Brunner J New photolabeling and crosslinking methods. Annu. Rev. Biochem. 62, 483–514, doi:10.1146/annurev.bi.62.070193.002411 (1993). [PubMed: 8352595]
42. Dochow M, Krumm SA, Crowe JE Jr., Moore ML & Plemper RK Independent structural domains in paramyxovirus polymerase protein. J Biol Chem 287, 6878–6891, doi:10.1074/jbc.M111.325258 (2012). [PubMed: 22215662]

43. Haller AA, MacPhail M, Mitiku M & Tang RS A single amino acid substitution in the viral polymerase creates a temperature-sensitive and attenuated recombinant bovine parainfluenza virus type 3. Virology 288, 342–350, doi:10.1006/viro.2001.1106 (2001). [PubMed: 11601905]
44. Leppert M, Rittenhouse L, Perrault J, Summers DF & Kolakofsky D Plus and minus strand leader RNAs in negative strand virus-infected cells. Cell 18, 735–747, doi:10.1016/0092-8674(79)90127-2 (1979). [PubMed: 229962]
45. Braun MR et al. RNA elongation by respiratory syncytial virus polymerase is calibrated by conserved region V. PLoS Pathog. 13, e1006803, doi:10.1371/journal.ppat.1006803 (2017). [PubMed: 29281742]
46. Behrens SE, Tomei L & De Francesco R Identification and properties of the RNA-dependent RNA polymerase of hepatitis C virus. EMBO J 15, 12–22 (1996). [PubMed: 8598194]
47. Noton SL, Deflube LR, Tremaglio CZ & Fearns R The respiratory syncytial virus polymerase has multiple RNA synthesis activities at the promoter. PLoS Pathog. 8, e1002980, doi:10.1371/journal.ppat.1002980 (2012). [PubMed: 23093940]
48. Jordan PC et al. Initiation, extension, and termination of RNA synthesis by a paramyxovirus polymerase. PLoS Pathog. 14, e1006889, doi:10.1371/journal.ppat.1006889 (2018). [PubMed: 29425244]
49. Madden JF, Burchette JL Jr. & Hale LP Pathology of parainfluenza virus infection in patients with congenital immunodeficiency syndromes. Hum Pathol 35, 594–603, doi:10.1016/j.humpath.2003.11.012 (2004). [PubMed: 15138935]
50. Toots M et al. Characterization of orally efficacious influenza drug with high resistance barrier in ferrets and human airway epithelia. Sci. Transl. Med. 11, doi:10.1126/scitranslmed.aax5866 (2019).
51. Balogh Sivars K et al. A 3D Human Airway Model Enables Prediction of Respiratory Toxicity of Inhaled Drugs In Vitro. Toxicol Sci 162, 301–308, doi:10.1093/toxsci/kfx255 (2018). [PubMed: 29182718]
52. Zhang L et al. Infection of ciliated cells by human parainfluenza virus type 3 in an in vitro model of human airway epithelium. Journal of virology 79, 1113–1124, doi:10.1128/JVI.79.2.1113-1124.2005 (2005). [PubMed: 15613339]
53. Karron RA & Collins PL in Fields Virology Vol. 1 (eds Knipe DM & Howley PM) Ch. 42, 1497–1526 (Wolters Kluwer/Lippincott Williams & Wilkins, 2007).
54. Mostafa HH, Vogel P, Srinivasan A & Russell CJ Dynamics of Sendai Virus Spread, Clearance, and Immunotherapeutic Efficacy after Hematopoietic Cell Transplant Imaged Noninvasively in Mice. Journal of virology 92, doi:10.1128/JVI.01705-17 (2018).
55. Burke CW, Li M, Hurwitz JL, Vogel P & Russell CJ Relationships among dissemination of primary parainfluenza virus infection in the respiratory tract, mucosal and peripheral immune responses, and protection from reinfection: a noninvasive bioluminescence-imaging study. Journal of virology 89, 3568–3583, doi:10.1128/JVI.03581-14 (2015). [PubMed: 25589649]
56. Wetzel JL, Fensterl V & Sen GC Sendai virus pathogenesis in mice is prevented by Ifit2 and exacerbated by interferon. Journal of virology 88, 13593–13601, doi:10.1128/JVI.02201-14 (2014). [PubMed: 25231314]
57. Sakaguchi T et al. Analysis of interaction of Sendai virus V protein and melanoma differentiation-associated gene 5. Microbiol Immunol 55, 760–767, doi:10.1111/j.1348-0421.2011.00379.x (2011). [PubMed: 21851384]
58. Garcin D, Latorre P & Kolakofsky D Sendai virus C proteins counteract the interferon-mediated induction of an antiviral state. Journal of virology 73, 6559–6565 (1999). [PubMed: 10400752]
59. Fulginiti VA, Eller JJ, Downie AW & Kempe CH Altered reactivity to measles virus. Atypical measles in children previously immunized with inactivated measles virus vaccines. Jama 202, 1075–1080, doi:10.1001/jama.202.12.1075 (1967). [PubMed: 6072745]
60. Kim HW et al. Respiratory syncytial virus disease in infants despite prior administration of antigenic inactivated vaccine. Am J Epidemiol 89, 422–434, doi:10.1093/oxfordjournals.aje.a120955 (1969). [PubMed: 4305198]
61. Ogino M et al. Vesiculopolins, a New Class of Anti-Vesiculoviral Compounds, Inhibit Transcription Initiation of Vesiculoviruses. Viruses 11, doi:10.3390/v11090856 (2019).

62. Duvall JR et al. Novel diversity-oriented synthesis-derived respiratory syncytial virus inhibitors identified via a high throughput replicon-based screen. Antiviral Res. 131, 19–25, doi:10.1016/j.antiviral.2016.03.015 (2016). [PubMed: 27059228]
63. Mason SW et al. Polyadenylation-dependent screening assay for respiratory syncytial virus RNA transcriptase activity and identification of an inhibitor. Nucleic acids research 32, 4758–4767, doi:10.1093/nar/gkh809 (2004). [PubMed: 15356293]
64. Cox RM et al. Development of an allosteric inhibitor class blocking RNA elongation by the respiratory syncytial virus polymerase complex. The Journal of biological chemistry 293, 16761–16777, doi:10.1074/jbc.RA118.004862 (2018). [PubMed: 30206124]
65. Tiong-Yip CL et al. Characterization of a respiratory syncytial virus L protein inhibitor. Antimicrob. Agents Chemother. 58, 3867–3873, doi:10.1128/AAC.02540-14 (2014). [PubMed: 24777090]
66. Ontoria JM et al. Identification and biological evaluation of a series of 1H-benzo[de]isoquinoline-1,3(2H)-diones as hepatitis C virus NS5B polymerase inhibitors. J. Med. Chem. 52, 5217–5227, doi:10.1021/jm900517t (2009). [PubMed: 19877603]
67. Ruebsam F et al. Pyrrolo[1,2-b]pyridazin-2-ones as potent inhibitors of HCV NS5B polymerase. Bioorganic & medicinal chemistry letters 18, 3616–3621, doi:10.1016/j.bmcl.2008.04.066 (2008). [PubMed: 18487044]
68. Fearns R & Deval J New antiviral approaches for respiratory syncytial virus and other mononegaviruses: Inhibiting the RNA polymerase. Antiviral Res. 134, 63–76, doi:10.1016/j.antiviral.2016.08.006 (2016). [PubMed: 27575793]
69. Liuzzi M et al. Inhibitors of respiratory syncytial virus replication target cotranscriptional mRNA guanylylation by viral RNA-dependent RNA polymerase. J. Virol. 79, 13105–13115, doi:10.1128/JVI.79.20.13105-13115.2005 (2005). [PubMed: 16189012]
70. Nair AB & Jacob S A simple practice guide for dose conversion between animals and human. J Basic Clin Pharm 7, 27–31, doi:10.4103/0976-0105.177703 (2016). [PubMed: 27057123]
71. Beaty SM et al. Efficient and Robust Paramyxoviridae Reverse Genetics Systems. mSphere 2, doi:10.1128/mSphere.00376-16 (2017).
72. Amonsen M, Smith DF, Cummings RD & Air GM Human parainfluenza viruses hPIV1 and hPIV3 bind oligosaccharides with alpha2–3-linked sialic acids that are distinct from those bound by H5 avian influenza virus hemagglutinin. Journal of virology 81, 8341–8345, doi:10.1128/JVI.00718-07 (2007). [PubMed: 17522226]
73. Jacob RT et al. MScreen: an integrated compound management and high-throughput screening data storage and analysis system. J. Biomol. Screen. 17, 1080–1087, doi:10.1177/1087057112450186 (2012). [PubMed: 22706349]
74. Greninger AL et al. Rapid Metagenomic Next-Generation Sequencing during an Investigation of Hospital-Acquired Human Parainfluenza Virus 3 Infections. J Clin Microbiol 55, 177–182, doi:10.1128/JCM.01881-16 (2017). [PubMed: 27795347]
75. Li H & Durbin R Fast and accurate short read alignment with Burrows-Wheeler transform. Bioinformatics 25, 1754–1760, doi:10.1093/bioinformatics/btp324 (2009). [PubMed: 19451168]
76. Koboldt DC et al. VarScan 2: somatic mutation and copy number alteration discovery in cancer by exome sequencing. Genome Res. 22, 568–576, doi:10.1101/gr.129684.111 (2012). [PubMed: 22300766]
77. Wang K, Li M & Hakonarson H ANNOVAR: functional annotation of genetic variants from high-throughput sequencing data. Nucleic Acids Res. 38, e164, doi:10.1093/nar/gkq603 (2010). [PubMed: 20601685]
78. Chi H et al. Comprehensive identification of peptides in tandem mass spectra using an efficient open search engine. Nat. Biotechnol, doi:10.1038/nbt.4236 (2018).

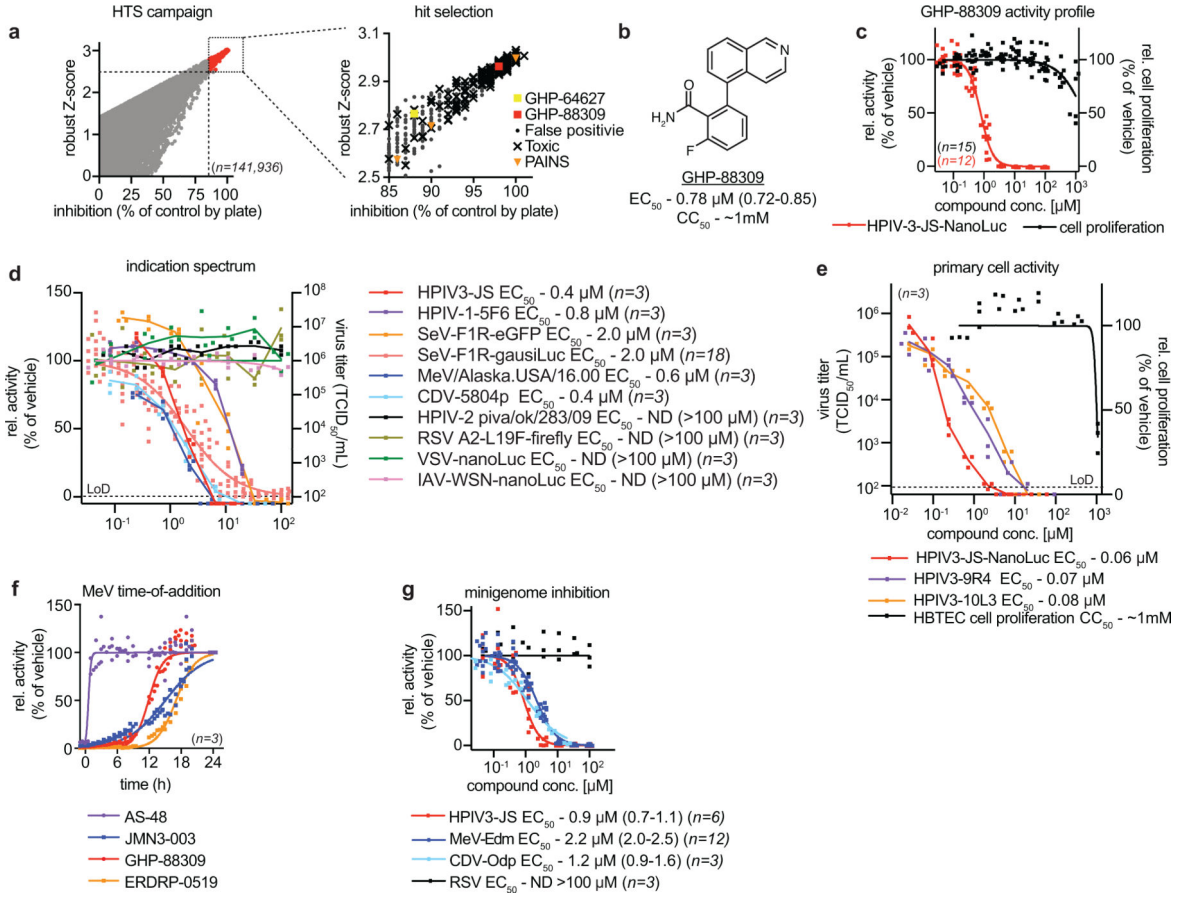

Fig. 1.

Identification and initial characterization of GHP-88309. **a,** Results of a primary HPIV3 HTS campaign and counterscreening of hit candidates (enlarged area). BEAS-2B cells were infected at MOI of 0.2 $TCID_{50}$ units/cell; final compound concentration was 5 µM; plates were read after 30-hour incubation; HTS was carried out as a single experiment (n=1). **b,** GHP-88309 chemical structure. **c,** Bioactivity (dose-response assay against recHPIV-3-JS-NanoLuc; MOI 0.2 $TCID_{50}$ units/cell) and toxicity (PrestoBlue-based cell viability assay) profiling of resynthesized GHP-88309; cell exposure times 48 hours. **d,** GHP-88309 has a broadened activity spectrum covering paramyxoviruses of two genera (left panel). Table summarizes EC_{50} and EC_{90} concentrations and SI values against different viral targets (right panel). **e,** Antiviral activity of GHP-88309 against clinical isolates of HPIV3 (MOI 0.1 $TCID_{50}$ units/cell) on disease-relevant primary human airway cells. Effects of GHP-88309 on cell proliferation was assessed on HBTECs (PrestoBlue assay); exposure times 48 hours. **f,** MeV ToA studies. Known MeV fusion (AS-48) and MeV polymerase (ERDRP-0519) inhibitors and a host-directed polymerase inhibitor (JMN3–003) are included for reference (20 µM final concentration each). **g,** Inhibitory activity of GHP-88309 against paramyxovirus and pneumovirus minigenome reporter systems. In (c-g), symbols represent biological repeats (n ≥3 throughout) and lines connect data means. Numbers specify EC_{50} concentrations calculated through 4-parameter variable slope regression modeling with 95% CIs in parentheses.

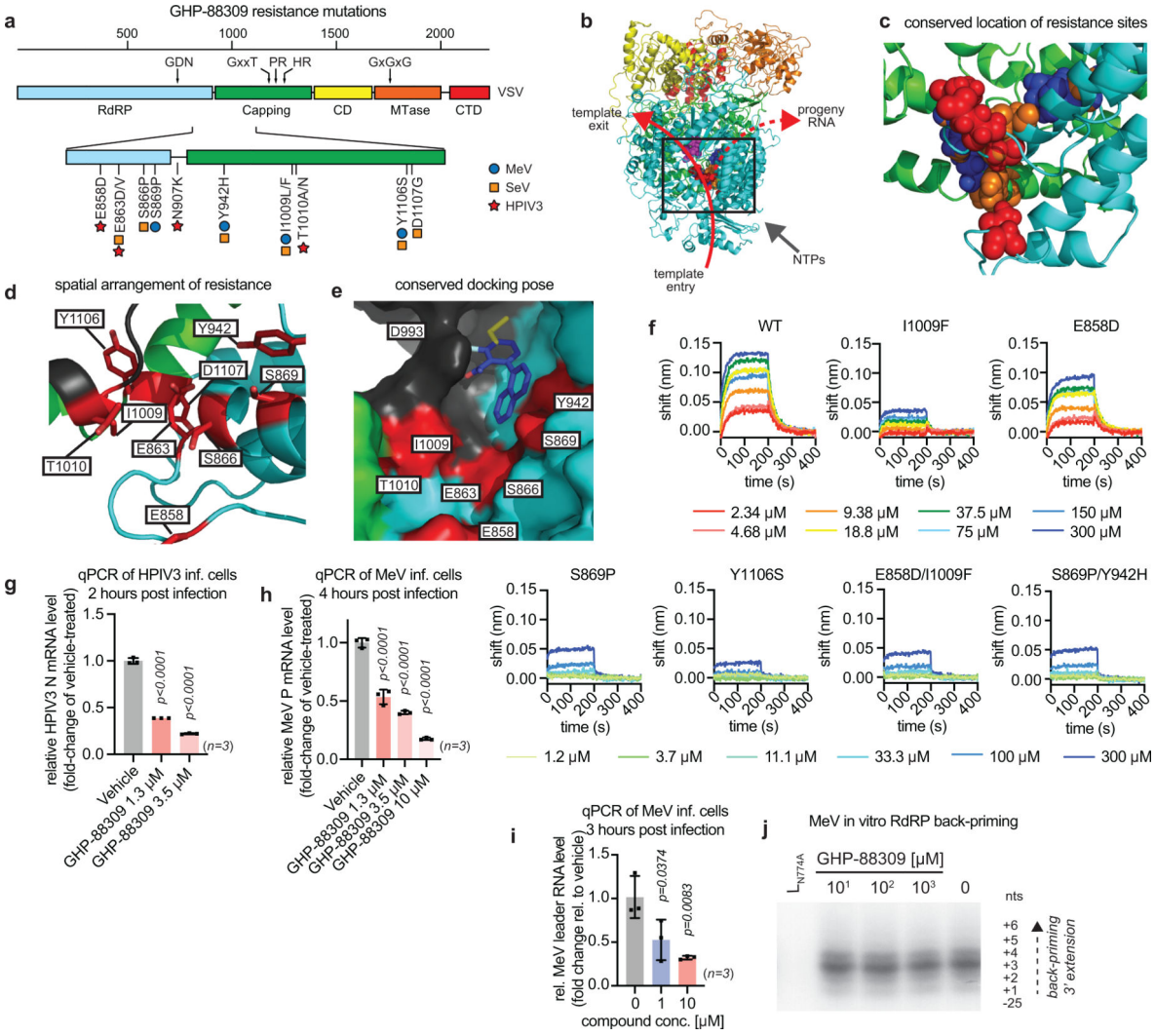

Fig. 2.

GHP-88309 targets a conserved microdomain in the L protein, inhibiting *de novo* RNA synthesis. **a,** Schematic of mononegavirus L (by example of VSV) and resistance mutations identified from adaptation of HPIV3, MeV, and SeV (shown in red, blue, and orange, respectively). CD: connector domain; MTase: methyltransferase; CTD: carboxy-terminal domain. **b-c,** Color-coded mapping of resistance mutations on a homology model of HPIV3 L based on HPIV5 L (PDB 6v85) (b). Resistance hot-spots locate between RdRP and capping domains in the template channel (HPIV3, red spheres; SeV, orange spheres; MeV, blue spheres); GDN active site is shown as purple spheres (c). **d,** Resistance mutations mapped on MeV L, based on HPIV5 L. **e,** *In silico* docking of GHP-88309 (blue sticks) into MeV L, depicted as surface colored by RdRP (cyan) and capping (green) domains. Shown are residues identified through photoaffinity labeling (black), resistance sites (red), GHP-88309–016 (yellow), and GHP-88309 (overlayed in blue). **f,** BLI of GHP-88309 and purified standard MeV L and L harboring selected resistance mutations. BLI studies were performed in two repeats with similar results (Source Data (Plemper_SourceData_Fig2_Originals_Repeats.pdf)). **g-h,** Inhibition of primary viral

mRNA transcription by GHP-88309 measured 2 (g; HPIV3) or 4 (h; MeV) hours after infection. **i,** Effect of GHP-88309 on relative MeV Le RNA concentration, measured 3 hours after infection. **j,** Autoradiogram of *in vitro* MeV RdRP assay products. GHP-883089 in escalating concentrations does not block 3´ RNA extension after back-priming. Inactive L_{N774A} served as specificity control. The experiment was performed three times with similar results (Plemper_SourceData_Fig2_Originals_Repeats.pdf). In (g-i), symbols represent biological repeats, columns show means ± SD. Significance was tested by one-way ANOVA with Dunnett's multiple comparisons post-hoc test (two-sided). Individual P values are shown.

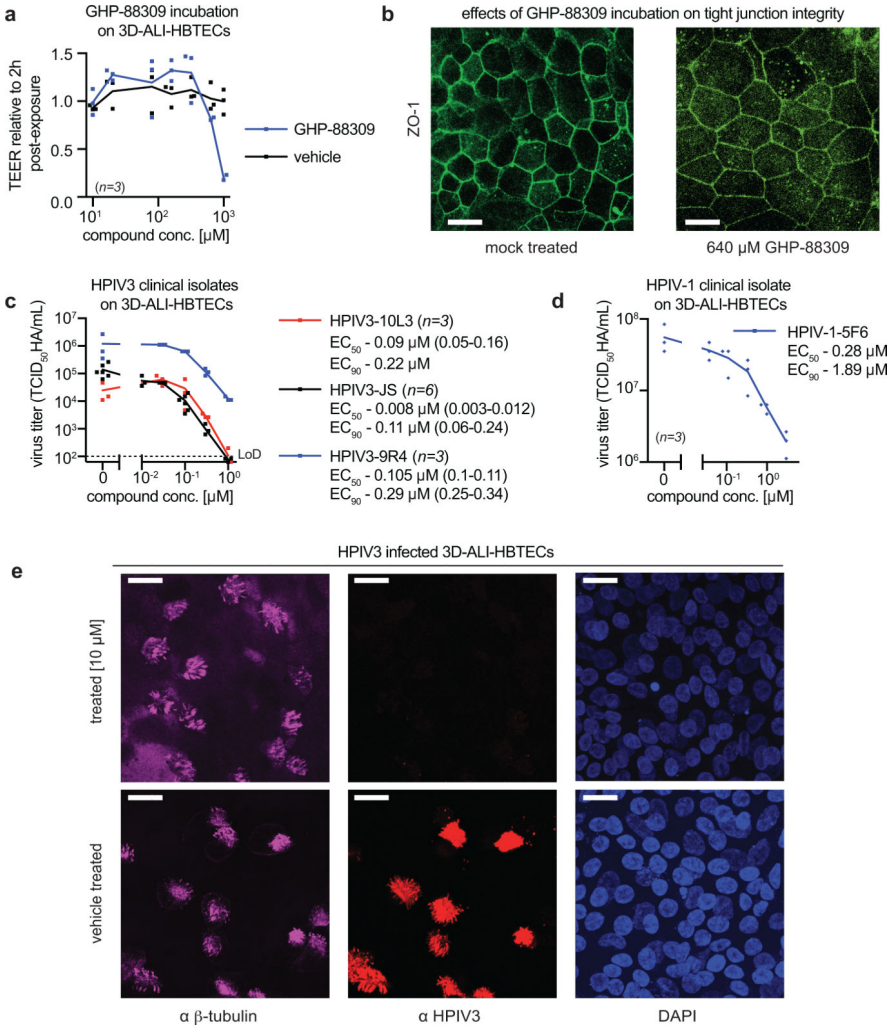

Fig. 3.

GHP-88309 is efficacious in well-differentiated human airway epithelium cultures grown at air-liquid interface (3D-ALI-HBTEC). **a,** Effect of increasing concentrations of GHP-88309 on trans-epithelial electrical resistance (TEER) in the 3D-ALI-HBTEC culture. **b,** Confocal microscopy examining tight junction integrity (α ZO-1) after incubation of 3D-ALI-HBTEC cultures with 640 μM GHP-88309. Two independent repeats, all originals are deposited at https://doi.org/10.6084/m9.figshare.12417266.v1. **c-d,** Antiviral potency of GHP-88309 against HPIV3 strain JS and two clinical HPIV3 isolates (10L3 and 9R4) (c) and clinical HPIV1 isolate 5F6 (d) in 3D-ALI-HBTEC cultures. Compound was added to the basolateral chambers at the specified concentration ranges. **e,** Confocal microscopy of HPIV3-JS-infected 3D-ALI-HBTEC cultures. Stained are ciliated cells (α β-tubulin), HPIV3 antigens (α HPIV3), and nuclei (DAPI). Scale bar 20 μm. GHP-88309 added to the basolateral chamber at 10 μM is sterilizing. Two independent repeats, all originals are deposited at https://doi.org/10.6084/m9.figshare.12417269.v1. In (a, c-d), symbols represent biological repeats, lines connect mean values. Active concentrations of GHP-88309 were determined through 4-parameter variable slope regression modeling (c-d).

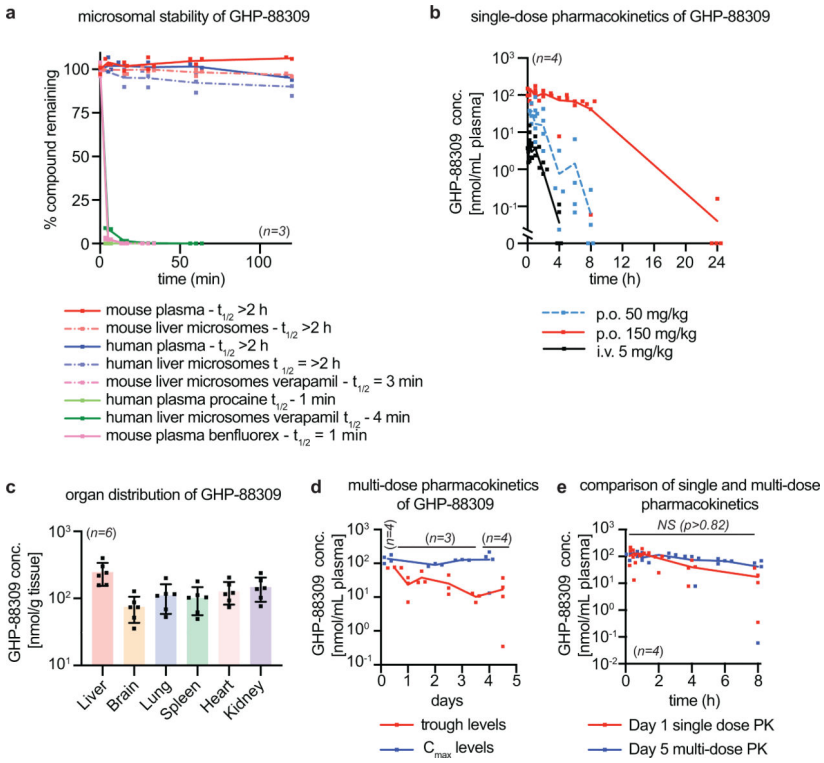

Fig. 4.

PK characterization of GHP-88309. **a**, Stability of GHP-88309 after incubation with mouse or human plasma, or mouse or human liver microsomes, respectively. Half-life ($t_{1/2}$) of GHP-88309 was estimated to be >15 hours in all conditions tested. Positive controls were procaine, benfluorex, and verapamil. **b,** Single-dose oral versus intravenous (i.v.) PK study of GHP-88309 in mice. **c**, Tissue distribution of GHP-88309 in mice. Specified tissues were extracted 90 minutes after a single oral dose at 150 mg/kg. Blood was sampled from 4 animals on days 0, 4 and 5, and from 3 animals on days 1–3. **d**, Blood drug concentrations after multi-dose administration of GHP-88309 to mice at 150 mg/kg, given orally b.i.d. for a total of 4.5 days. Blood was collected at peak (C_{max}; 0.5 hours after dosing; blue) and trough (11.5 hours after dosing; red). **e,** Comparison of mouse blood PK curves after single (red) and multi (blue) oral dosing of GHP-88309 (150 mg/kg). Multi-dose animals from (d), samples on day 5 after initiation of dosing. Statistical analysis through two-way ANOVA with Sidak's multiple comparisons post-hoc test. Throughout, symbols represent biological repeats, lines connect mean values (a-b, d-e). Columns represent data means ± SD (c).

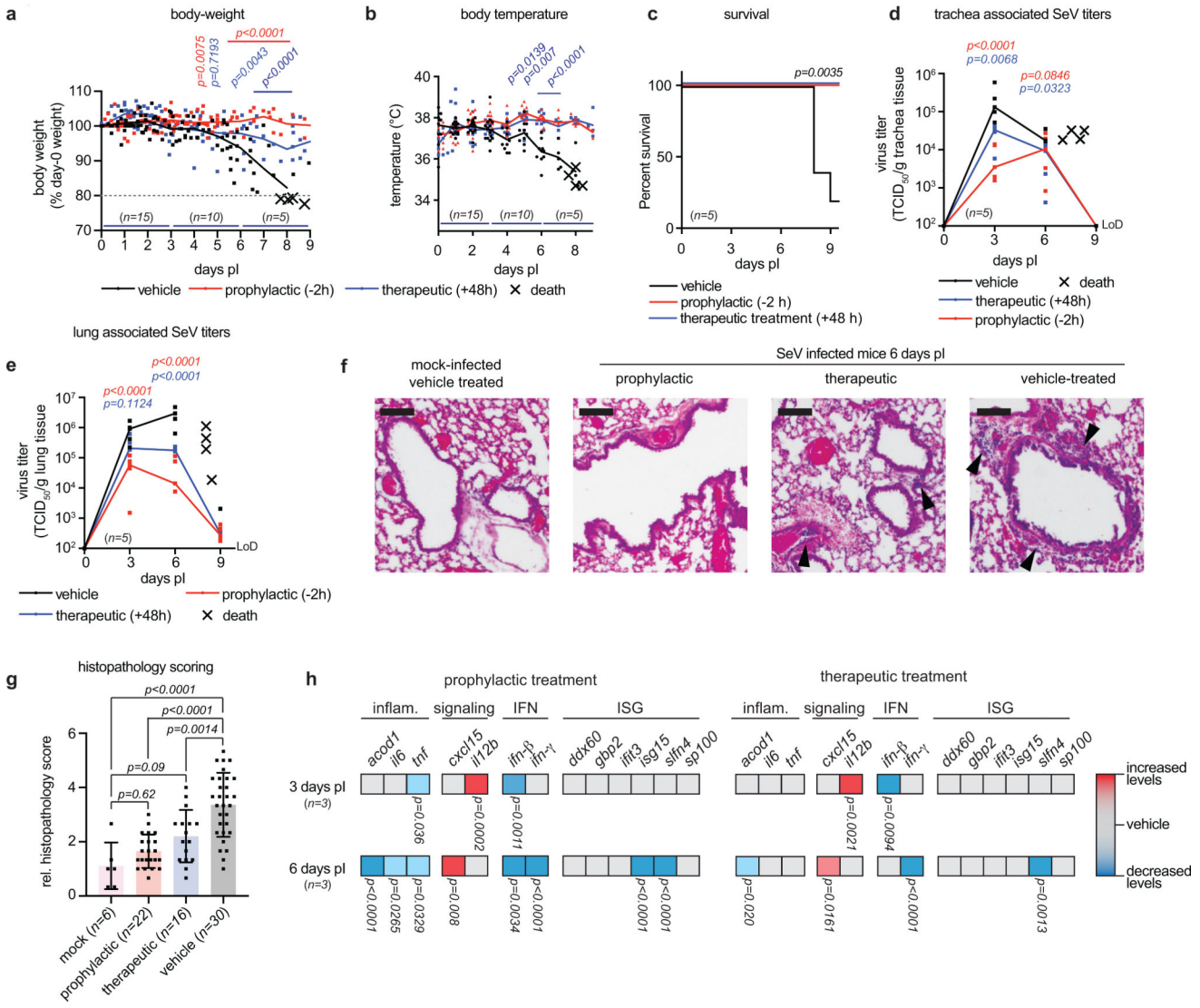

Fig. 5.

GHP-88309 is efficacious in a SeV mouse surrogate assay of HPIV infection. **a-e,** Oral efficacy of GHP-88309 after b.i.d. dosing of mice infected intranasally with 1.5×10^5 $TCID_{50}$ units of SeV at 150 mg/kg. Treatment was initiated two hours before (prophylactic) or 48 hours after (therapeutic) infection. Clinical signs (body weight (a) and temperature (b)) were monitored daily. Survival (c) was calculated nine days after infection. Analysis through time-to-event log-rank (Mantel-Cox) test. On days 3, 6, and 9 after infection (days pI), virus burden in trachea (d) and lungs (e) were determined. Symbols represent individual animals, lines connect medians. Statistical analysis through two-way ANOVA with Dunnett's multiple comparisons post-hoc test (two sided). **f**, Representative lung sections after H&E staining of mock or SeV-infected mice, treated with GHP-88309 as in (a-e). Lungs were extracted from three animals per condition six days after infection. Scale bars represent 100 μm. Black arrows point to sites of immune infiltration. Originals are deposited at 10.6084/m9.figshare.12417275. **g**, Histopathology scores of lung sections from all animals as shown in (e). Per condition, >16 distinct sections of three animals were analyzed. For mock

infected vehicle treated images, six distinct sections were used from one mouse. Symbols represent individual histopathology scores, columns show means ± SD. Statistical analysis through one-way ANOVA with Tukey's multiple comparisons post-hoc test. Histopathology slides are deposited at 10.6084/m9.figshare.12417239. **h**, Heat maps of relative mRNA amounts of selected host genes associated with antiviral response pathways in mice of the prophylactic and therapeutic treatment groups, all shown in relation to vehicle-treated mice on days 3 and 6 after infection, respectively. Color-coding denounces significantly higher (red), lower (blue), or unchanged (grey) mRNA amounts relative to the vehicle-treated animals. Statistical analysis through one-way ANOVA with Dunnett's multiple comparisons post-hoc test (two-sided).

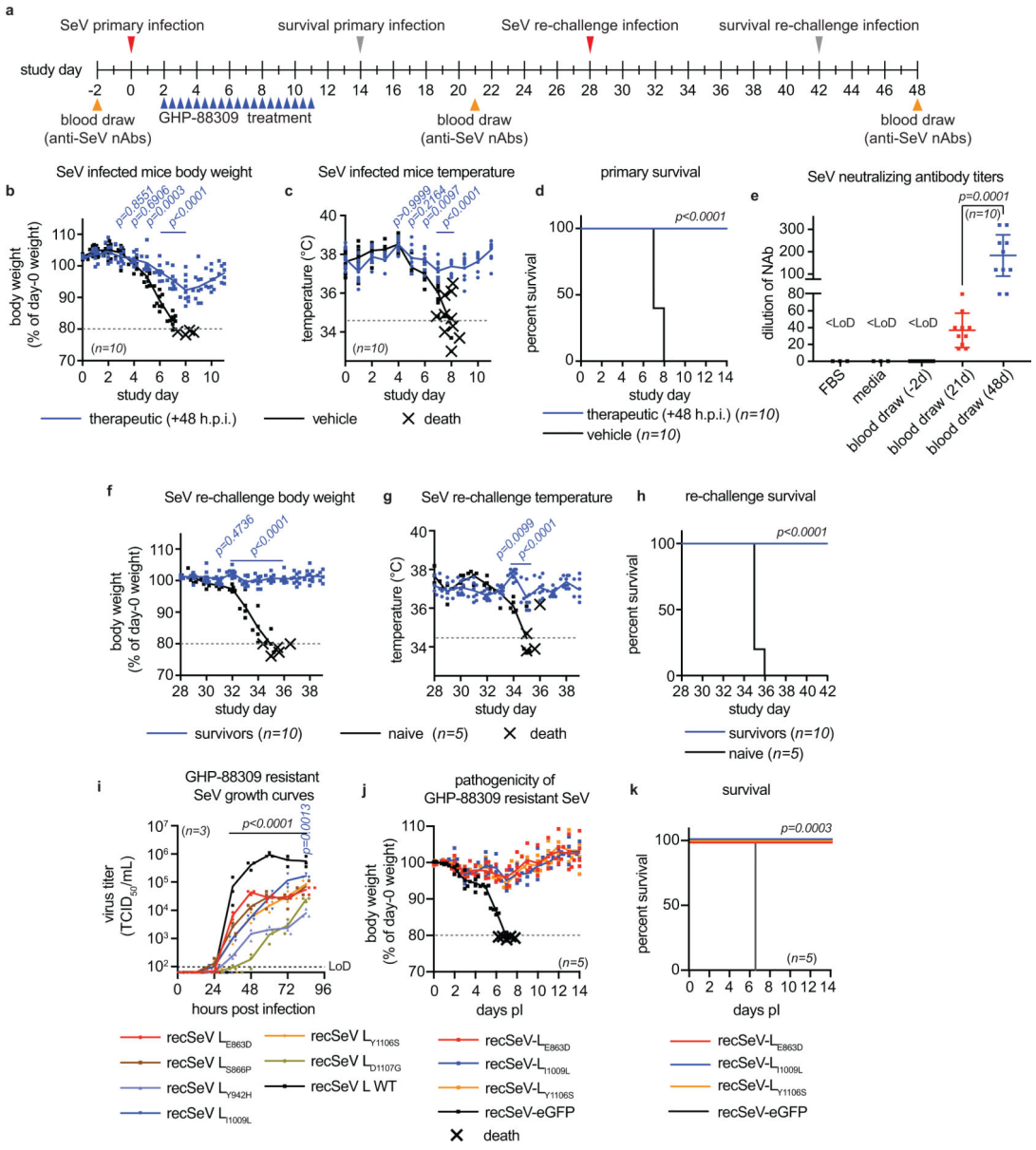

Fig. 6.

Effect of GHP-88309 treatment on adaptive immunity and rechallenge, and correlation between resistance and viral pathogenesis*.* **a,** Schematic of long-term survival and rechallenge study. Animals were treated therapeutically with GHP-88309 at 150 mg/kg dose concentration, administered b.i.d. **b-c,** Daily monitoring of clinical signs (body weight (b) and temperature (c)) after initial challenge with 1.5×10^5 $TCID_{50}$ units of SeV administered intranasally. **d,** Survival curve of SeV-infected mice after primary infection and therapeutic (+48 hours after infection) GHP-88309 treatment. **e,** Assessment of neutralizing antibodies directed against SeV of mice before treatment (blood draw (−2 days)), before rechallenge (blood draw (21 days)), and after rechallenge (blood draw (48 days)). Neutralizing effects of FBS and culture media (media) were tested for control. **f-g,** Intranasal rechallenge of recoverees from (b) with a 1.5×10^5 $TCID_{50}$ of SeV on day 28 after the primary infection.

Monitored were clinical signs (body weight (e) and temperature (f)). For reference, a fresh group of naïve mice was infected equally in parallel. **h,** Survival curves of SeV-infected mice from (f-g). **i,** Growth curves of standard recSeV and recSeVs with confirmed GHP-88309 resistance mutations in cultured cells. **j-k**, Effect of resistance mutations on SeV pathogenesis in mice. Daily monitoring of body weight (i) and overall survival (j) after intranasal infection with 1.5×10^5 $TCID_{50}$ of standard recSeV or three distinct recSeVs with the specified signature resistance mutations. Throughout, symbols represent biological repeats, lines indicate means (b-c; e-g; j) or medians (i). Error bars in (e) show SD. Statistical analysis through two-way ANOVA and Sidak's multiple comparisons post-hoc test (b-c, f-g, i) or unpaired two-sided t-test (e). Statistical differences in time-to-death were explored through log-rank (Mantel-Cox) test (d, h, k).

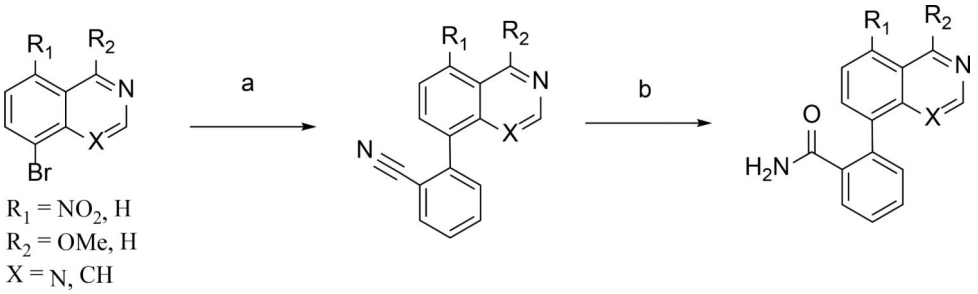

R_1 = NO_2, H
R_2 = OMe, H
X = N, CH

Scheme 1:

Reagents and Conditions: a) (2-cyanophenyl)boronic acid, $Pd(PPh_{3)4,}$ $Na_2CO_{3,}$ Dioxane, H_2O,100 °C, 3 hr; b) AcOH, Conc. $H_2SO_{4,}$ 120°C, hr.

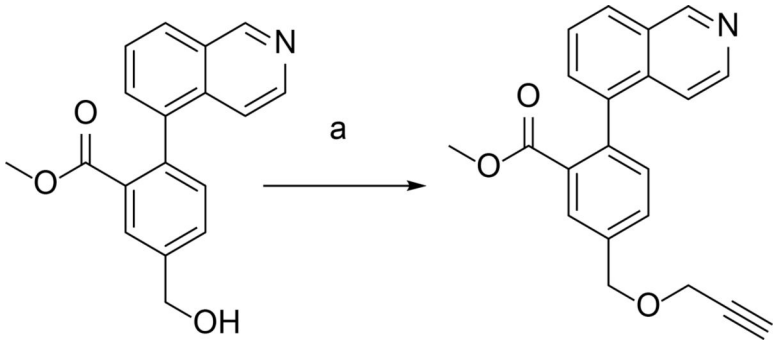

Scheme 2:

Reagents and Conditions: a) Propargyl bromide, NaH, DMF.

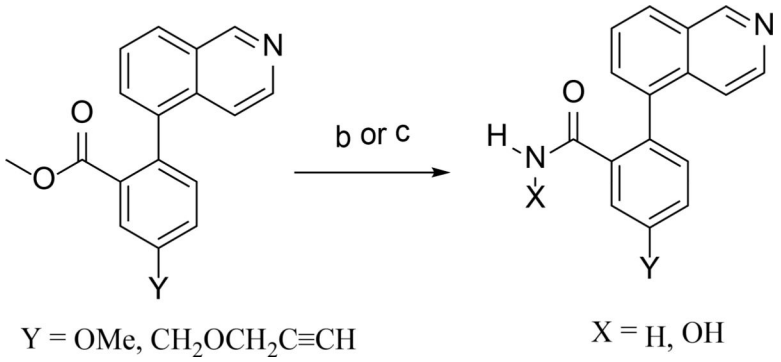

Y = OMe, $CH_2OCH_2C{\equiv}CH$ X = H, OH

Scheme 3:

Reagents and Conditions: b) NH_3, M_eOH, N_aCN, sealed tube, 90 °c, 24hr; c) NH_2OH, KOH, (1:)(THF:M_eOH)